UNIVERSITY OF TURKU

Characterization of Organic Light Emitting Diodes

Department of Mechanical Engineering, Faculty of Technology

Master of Science in Technology Thesis

Author:
Santeri Kanerva

February 2026

Turku

Supervisors:
Assoc. Prof. Konstantinos Daskalakis
Asst. Prof. Mohsen Amraei
Postdoc. Henri Lyyra

The originality of this thesis has been checked in accordance with the University of Turku quality assurance system using the Turnitin Originality Check service.

Master's thesis

Subject: Mechanical Engineering
Programme: Master’s Degree Programme in Mechanical Engineering
Author: Santeri Kanerva
Title: Characterization of Organic Light Emitting Diodes
Number of pages: 30 pages, 11 appendix pages
Date: March 2026

Technology behind Organic Light Emitting Diodes (OLEDs) is under intense development, as the drive for more efficient light sources is accelerating due to environmental and economic concerns. However, the emission profiles of devices with novel organic materials and photonic structures require angle-resolved spectroscopic characterization to determine device performance accurately. This thesis details the design, fabrication, and validation of a custom, reconfigurable goniometric system capable of semi-circular spectroscopic scans with an angular resolution of 0.45 degrees. Additionally, a temporary encapsulation method for research OLEDs is presented. Using the developed system, an electroluminescent scan was performed on a blue OLED, revealing a non-Lambertian emission profile. These results were used to derive a shape correction factor of approximately 1.7, which could be used to accurately calculate the External Quantum Efficiency (EQE).

Key words: OLED Characterization, Goniometer Design, Angle-Resolved Electroluminescence

Table of contents

1 Introduction

Artificial light—for all the good it brings—contributes a major portion of the global greenhouse gas emissions and represents a substantial economic burden, and the drive for large quantities of better and more affordable light sources is constantly growing.

The global economic and environmental costs of lighting technology are notable: In 2023, homes in the European Union (EU) used 14.5 % of their total electricity consumption to power lights and electrical appliances. This amounted to a total of 390 billion kilowatt-hours (kWh), costing approximately €94 billion. In 2018, commercial buildings and manufacturing facilities in the United States (US) consumed a total of 261 billion kWh to power their lights. The electricity usage at that time in the US generated emissions of 463 grams of CO2 per kWh from all combined sources. This means that the US released 121 million metric tons of CO2 to power the lights of commercial and industrial buildings alone, while spending $25.9 billion. [1–5]

As display devices are ubiquitous and are composed of light emitting devices, they must be discussed. Most modern displays suffer from low efficiency: a typical display receives an EPREL energy label from D to G (the scale runs from A to G, from best to worst), with average power consumption of 26.3 kWh/1000h [1]. The European Comission reports 85 million monitors in use in EU countries, and that the average on-mode time for displays was 8.5 hours a day in 2025 [2]. The use of these displays results in an annual electricity consumption of 7 billion kWh, costing €2 billion and emitting 1.3 million metric tons of CO_2. As this represents only a small subset of displays in use, major savings in both financial and environmental terms can be realized even with modest efficiency improvements.

Modern light sources are increasingly often made of Light-Emitting Diodes (LEDs). This shift is driven by the fact that the increase in luminous efficacy of earlier technologies plateaued, which intensified research into LED performance. While LEDs made of inorganic semiconductors became commercially viable for general space-lighting in the early 2000s, the organic counterpart (OLED) still lags behind because it was discovered later and has not yet matured in terms of materials science and engineering [3,4]. An ongoing trend with LED development from the 1990’s onwards is that the luminous efficacy of the devices rise 10 lm/W every year, and the reported efficacies have risen from 10 to over 200 lm/W. [5]

The dramatic increase in device efficiency and lifetime together with the decrease in unit cost of LEDs have made them ubiquitous in most lighting applications. The technology has risen to such importance that many governments are phasing out others, and the LED is becoming the standard for most solutions for generating light [6–8].

Because of the difference in technology maturity, the luminous efficacy or device lifetime of OLEDs has not yet caught up to inorganic LEDs, which is why OLED technology is not as proliferated. Work is being done to find optimizations to materials and device structures that would increase the photonic yield and lifetime. Companies like LG Chem and Ikea have already experimented with indoor lighting products made with OLEDs: Ikea's first OLED lamp included multiple large-area panels and had a luminous efficacy of 77 lm/W. [9–11]

Regardless of inefficiency, the use of OLEDs over LEDs is already in many cases favorable to use in display devices due to their superior color quality to Liquid Crystal Displays (LCDs) or LED displays. Unlike conventional LCDs, an OLED display does not require a backlight. The dark parts of an image are created simply by switching off the corresponding OLED sub-pixels, so each pixel can emit light or be completely dark. This self-emissive architecture allows OLED panels to produce true "perfect blacks," whereas LCDs rely on a continuously active backlight that inevitably leaks some light and prevents a completely black level. Other advantages of OLEDs over LEDs are the optical transparency of the devices and their mechanical flexibility—showing the potential for flexible and curved displays, such as those seen in current (2026) folding phones. [12,13]

Another part of the OLED problem is their manufacturability. As stated earlier, the materials science and manufacturing engineering in this field are relatively immature. Many materials and their functional and manufacturability characteristics are yet to be explored. New ways of exploiting these characteristics to yield better devices are under intense development.

Whether the methods and materials used to manufacture state-of-the-art OLEDs yield improvements over previous iterations must be verified through quantitative characterization. The aim of this thesis is to develop a measurement system—including a mechanical setup, and a data acquisition and processing system—that allows for angle-dependent spectroscopy of an OLED in a non-reactive environment.

The thesis is outlined as follows: section 2 provides an introductory view of both organic and inorganic semiconductors, as well as theory behind OLEDs and their efficiency. Section 3

describes the process of designing and building a goniometric measurement setup along with a device or substrate sample holder. Section 4 describes experimentation and the gathered data is interpreted. The thesis is finally concluded in section 5.

2 Semiconducting materials and devices

This chapter gives a quick overview of semiconductor materials and goes into some detail in OLED architecture.

2.1 Semiconductors

Semiconductors are a class of materials that have electrical conductivities between that of conductors and insulators. The typical conductivities, defined as the reciprocal ohm meter ($[\Omega * m]^{-1}$), of insulators, semiconductors and conductors range from 10^{-17}, 10^{-4} and 10^{7}, respectively [14–16].

Charge mobility is facilitated by available atomic states outside of the valence: energy, whether in the form of thermal or electrical, must be input into the system to promote the charge carriers to the conducting state. The unit of energy that's generally used in this discussion is the electron volt (eV).

The electron structures of individual atoms consist of discrete energy states associated with different electron orbitals. When the atoms are brought together to form a bulk, their electrons—due to the Pauli exclusion principle—begin to occupy slightly different energy states. For an object of macroscopic size, the energy states are so closely spaced and numerous that they can be considered to form a continuum. At equilibrium, the total energy between the least and most energetic states forms what's called an energy band. Figure 1 displays this graphically. [17,18]

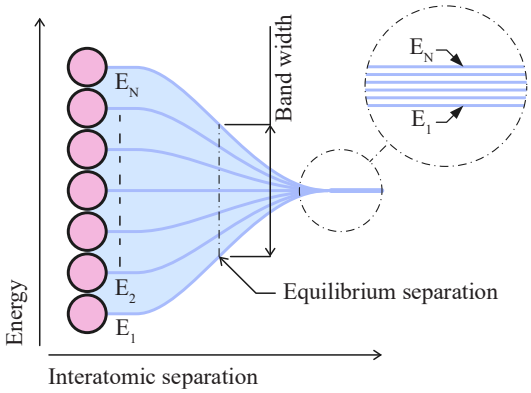

Figure 1. Energy band formation. Due to the Pauli exclusion principle, electrons of similar spin and spatial location cannot occupy the same energy states, so each electron begins to occupy slightly different states in the same bulk. When considering a macroscopic object where the number of atoms becomes extremely large, the difference in energy between them becomes very small. Because there are so many atoms, they collectively span some magnitude in energy, and because of the number of atoms, this span is effectively continuous. The magnitude of this span is called the band width of that energy band.

For metals, the free conducting states are either right next to or overlapping with the valence band. Even as temperature approaches 0 °K, the electrons can still transit into a conducting state. Polymers and ceramics are typically bad conductors, since practically all their electrons are tightly bound to individual atoms, and free conducting states lie beyond an insurmountable bandgap. The energy required to promote enough electrons into the conduction band of an insulator is impossible to reach with thermal excitation. An insulator may be categorized by a bandgap larger than 3 eV [18].

Semiconductor materials also have energy gaps between their valence and conduction bands, meaning that near 0 °K, they are not intrinsically useful conductors. The band gaps of semiconductors are much smaller than in insulators, between 0.1–3 eV. The smaller band gaps—and the thermal stability of the materials—mean that sufficient energy can be achieved by thermal excitation to promote electrons to the conduction band. Typical band structures for different materials are schematically shown in Figure 2. [18]

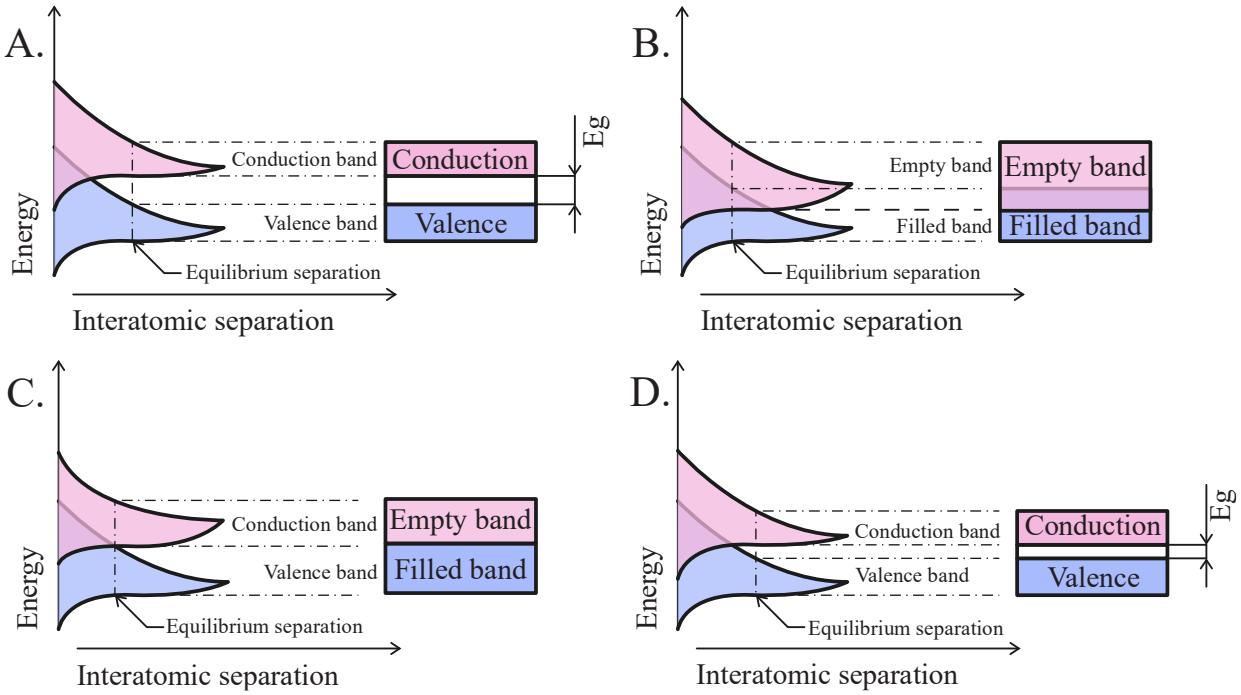

Figure 2. Typical band structures for different materials: (A) Insulator, (B, C) metal, and (D) semiconductor. The band widths at equilibrium separation are projected to the right to form a column-like graph. This is the conventional way of representing the band structure of a material.

Usually, the semiconductor materials need to be modified for them to be truly useful. For silicon, only at 400 °K, sufficient thermal energy is reached such that the electrons may transition the band gap, and charge carrier concentration begins to rise. The temperatures required for silicon and other pure semiconductors are therefore impractical for most uses.

Impurity materials are selectively introduced in a process called doping, to act as either donors (n-dopants) or acceptors (p-dopants); their occupied energy states lie in the host material's band gap, either close to the valence band or conduction band, depending on donor type. Donor molecules introduce states just below the conduction band, requiring minimal energy to promote an electron. Acceptor molecules lie near the valence band, where they accept electrons to leave behind conducting holes. A hole, in essence, is a vacancy in the electron structure of the material and can be considered as a charge carrying particle. In an electric field, a hole will allow electron movement in the valence band and thus partakes in conduction. Figure 3 explains doping semiconductors. [14]

The ability to dope semiconductors is what gives them their most useful properties. The LED is a doped semiconductor device: it works by having opposingly doped sides in the same substrate. Applying an electric bias with the correct polarity initiates current flow; electrons and holes meet at the junction and recombine radiatively.

The preceding discussion has been about inorganic semiconductor materials. The following will concentrate on their organic counterparts. Organic semiconductors function similarly to inorganics on a macroscopic level, but their molecular structure and the way they produce the semiconducting effect differs. Inorganic semiconductors form highly ordered lattices with strong covalent, metallic and ionic bonds, and conducting free electrons form what's termed an "electron gas"; the free electrons aren't bonded to any one atom and are free to move in the volume. Organic semiconductors, however, are either polymeric chains, molecular lattices or

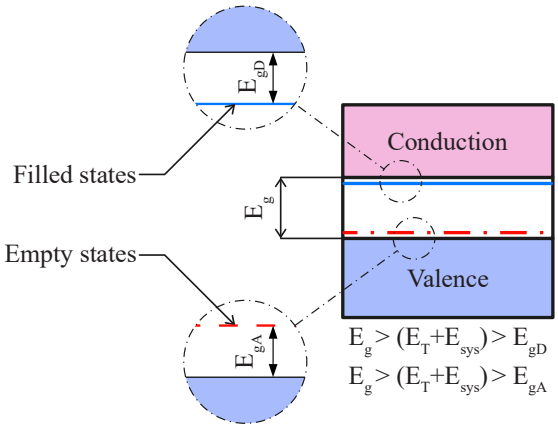

Figure 3. Band structure for an arbitrary doped semiconductor. The material is doped with molecules that have energy states close to the valence and conduction bands, inside the host material's forbidden zone. The valence and conduction bands of the host are separated by a band gap energy E_g. Donor and acceptor gaps to the host material's bands are shown as E_{gD} and E_{gA}, respectively. E_{sys} refers to the system energy near T = 0 °K. The increase in energy gained from ambient heat is enough to excite electrons from the host valence band to the empty acceptor dopant band, or from the donor dopant band to the host conduction band.

amorphous films that bond together by Van der Waals interactions; the key distinction is the carbon backbone structure and lack of strong bonds. Charge transport within an individual molecule is facilitated by conjugated π-bonds, where overlapping p-orbitals create a delocalized electron system along the carbon backbone. Charge transport between adjacent molecules or polymer chains happens by electron hopping, a process that's much less efficient than free electron movement in a crystalline material. Because the individual molecules are separated, distinct energy bands aren't created. Instead, each molecule has a Highest Occupied Molecular Orbital (HOMO) and a Lowest Unoccupied Molecular Orbital (LUMO). The energy difference between these is considered the band gap, and the effect is analogous to the band structure of inorganic semiconductors. Figure 4 compares an inorganic semiconductor's crystal lattice to a single organic semiconductor molecule. [19–23]

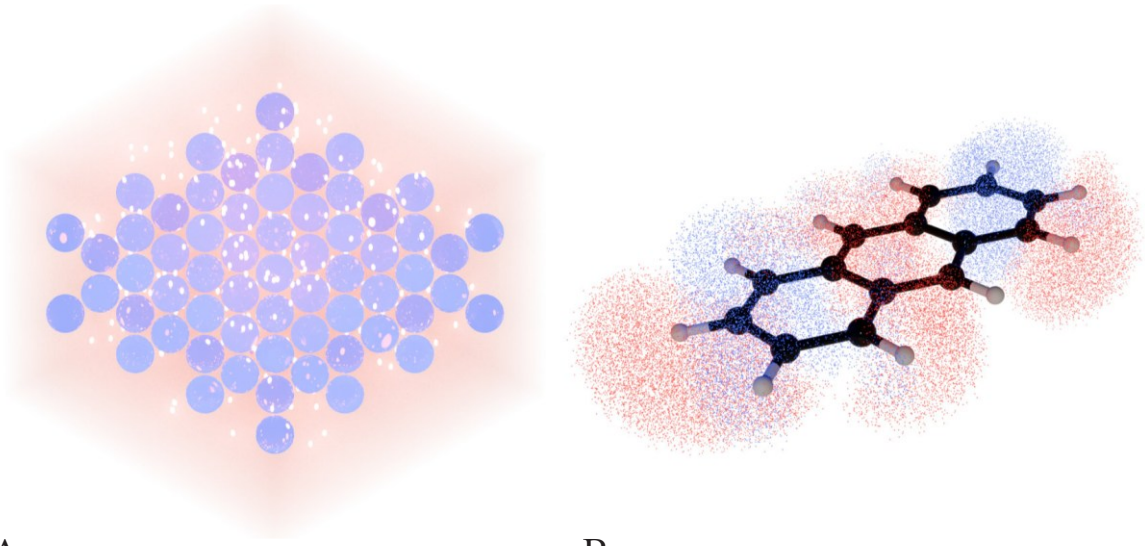

A. B.

Figure 4. An illustration of (A) "electron gas" in a Si lattice, and (B) the LUMO-orbital of an anthracene molecule.

The lack of strong bonds within organic semiconductors is one of the key advantages and disadvantages of the materials: they are, by nature, flexible and able to conform to and work on irregular surfaces, enabling flexible and curved electronics to be manufactured—whereas inorganics rely on rigid and planar substrates. The disadvantage, however, is that the lack of strong bonds and the disordered, low packing density structure allow easy access for foreign species like oxygen and water—which the materials are very sensitive to. An engineering challenge when manufacturing organics is then to protect them from exposure to outside elements. [11,19]

Another advantage of organic materials is their ability to be cost-effectively and quickly fabricated into thin films by solution processing methods. The active molecules of a device

can be dissolved and deposited onto a substrate with spin coating, spraying or inkjet-type printing methods. Expensive vacuum deposition equipment is not always needed, but for nanometer-level precise films, chemical vapor deposition, physical vapor deposition and sputter coating is typically used. [19]

2.2 The OLED

OLEDs are manufactured by thin film deposition of layers of different materials. Between two electrodes are layers of organic materials with unique characteristics in either transporting charges or converting them to radiation. OLEDs are categorized as either top-emitting or bottom-emitting—corresponding if the emission is through the substrate or the last deposited layer—which impacts the choice of electrode materials: the emitting side must be at least partially transparent to the generated wavelength spectrum.

The simplest practical OLED—first presented by Tang and VanSlyke in 1987—is composed of the substrate, the electrodes, and in between the electrodes two organic layers: the Hole Transport Layer (HTL) and the Emissive Layer (EML). As a forward bias is introduced, electrons from the cathode and holes from the anode are injected and transported into the EML, where they meet, recombine into an exciton and radiatively relax back to the ground state. This OLED is schematically presented in Figure 5. [4]

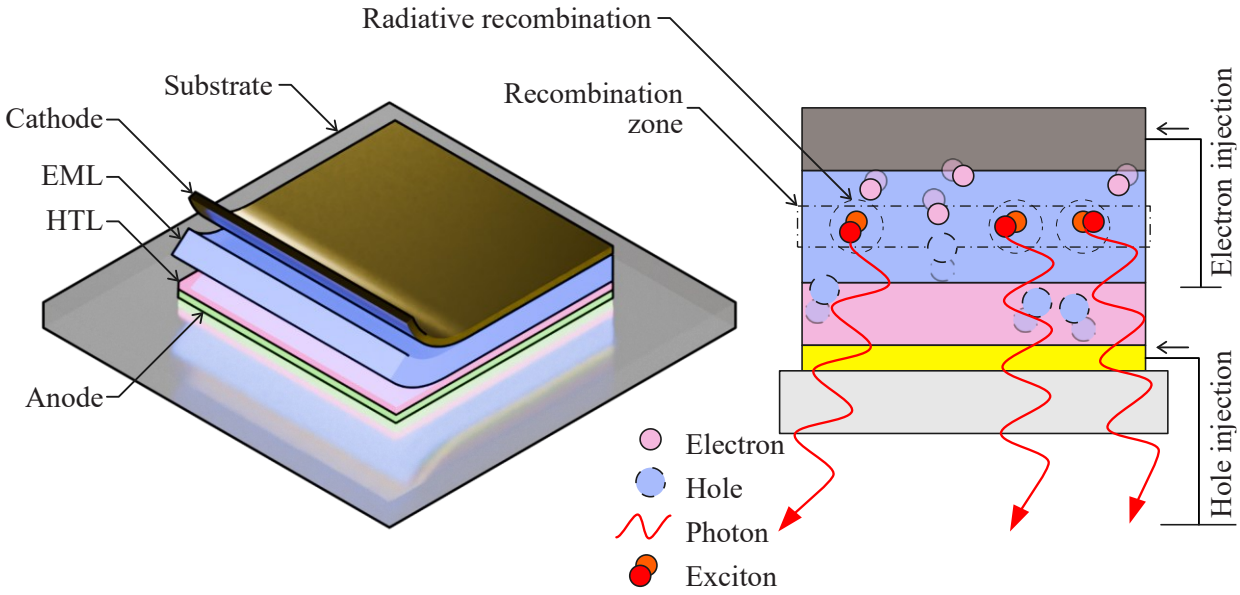

Figure 5. A schematic of the simplest practical OLED. The device is composed of the electrodes, a hole transport layer (HTL), and a single emissive layer (EML). Layers in the isometric projection are shown 'peeled back' to better illustrate them. The layer thicknesses are also exaggerated in the figure: typical layer thicknesses in an OLED range from tens to hundreds of nanometers.

A modern OLED will contain multiple organic layers with different purposes. The anode-HTL-EML-cathode stack is inefficient because most of the electrical current leaks through the device. The different organic layers act as charge carrier transporters or blockers. Their function is to ensure that charge carriers stay in the emissive region, thus increasing the probability of recombination. They achieve this by having tailored HOMO/LUMO levels. The layers and their abbreviations are summarized in Table 1. [24]

Table 1. Organic layers in OLEDs. For specific devices and applications, layers can be removed and layers with different functions can be added.

Layer	Abbreviation
Electron Transport Layer	ETL
Electron Blocking Layer	EBL
Emissive Layer	EML
Hole Transport Layer	HTL
Hole Blocking Layer	HBL

Since the HOMOs of the layers house localized electrons that do not participate in conduction, the electrons that are injected from the cathode travel in the LUMOs. It is

therefore beneficial for the ETL and HBL to have a deeper[1] LUMO, or one that is matched to the cathode's work function. The EBL will conversely have a very shallow LUMO, such that the energy barrier becomes too large to overcome for the electron in the EML. For hole transport, it is beneficial for a layer to have a shallower HOMO energy. This is because the lower energy vacancy will easily switch places with a higher-energy electron in the adjacent layer. A hole blocking layer will have a deep HOMO; since the energy is higher, the electron in the next layer can't overcome the barrier to switch places with the hole, thus confining the hole to the EML. Because both charge carriers are now confined and spatially overlapping in the same layer, they are more likely to recombine into an exciton. The energy level alignment of the device stack is schematically illustrated in Figure 6.

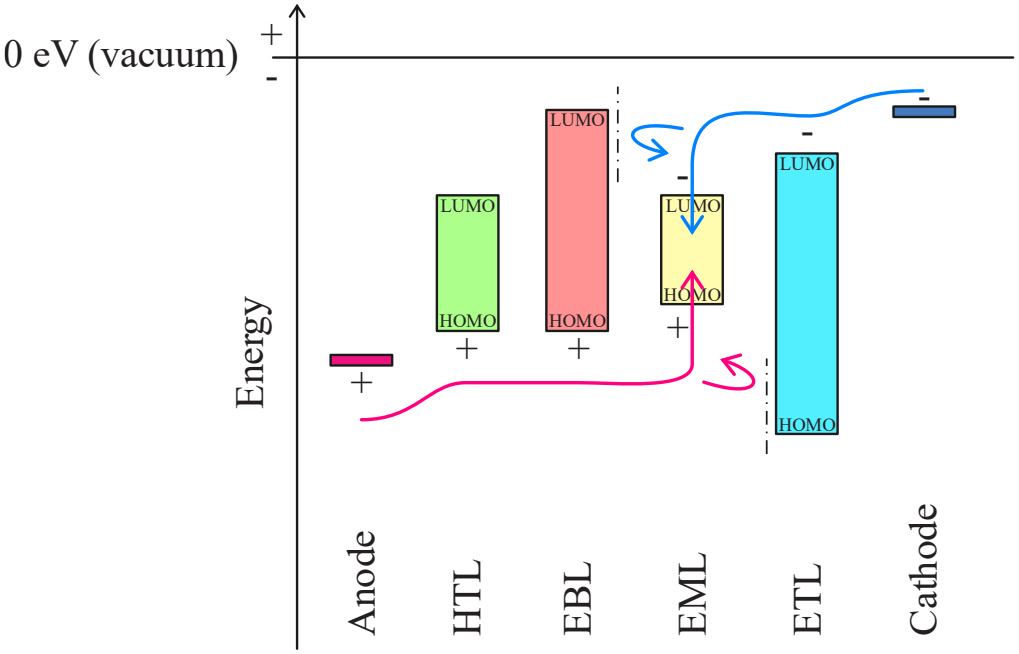

Figure 6. Schematic energy diagram of an OLED. The device stack is engineered to funnel charge carriers into the EML while preventing leakage current. Holes naturally migrate from lower to higher energy states, from deep to shallow HOMO levels. Introducing a layer with a deeper HOMO energy creates a barrier that blocks hole transport. Electrons naturally relax towards lower energy states; thus, a layer with a shallower LUMO energy acts as an electron blocking barrier. This confinement maximizes the probability of radiative recombination.

[1] The energy levels are described in reference to the vacuum energy, or the energy of an unbound electron. The energies of bound electrons within the materials are lower. When these energy levels are graphed, they are described analogously as being either shallow or deep.

2.3 Efficiency and dispersion of an OLED

As with any electronic device, the efficiency in converting electricity to useful energy is extremely important. In the case of OLEDs, efficiency is measured in two ways: luminous efficacy quantifies the ability of the device to turn electrical power to visible light. External Quantum Efficiency (EQE) is a unitless measure of how many photons in the desired spectrum are outcoupled per injected charge. Luminous efficacy is a useful measure when general lighting or display technology is discussed. EQE is a useful measure both within and outside the visible range.

Internal Quantum Efficiency (IQE) quantifies how many photons are generated per injected charge. OLED devices with IQEs approaching unity have already been developed, but current (2026) literature shows that device EQEs stay well below 50 % [25]. This is caused by difficulties in outcoupling the generated photons: some of the emitted light gets trapped within the device. A portion of any emitted light incident on any refractive interface—particularly the boundary between the device and air—reflects back into the stack where it can be reabsorbed and dissipated as heat. Light that is emitted over the critical angle will bounce between the electrodes or other layers and either escape through the edges of the device—that is, not in the viewing direction—or get reabsorbed. Propagation modes like this are termed waveguided modes. Light can also get trapped in plasmonic modes, where it interacts with the electrons of one of the metal electrodes and travels parallel to the surface. Several ways can be employed to mitigate these problems, including index-matching of different layers and modifying the optics of the device. [26]

The outcoupling efficiency has also been improved by incorporating photonic structures within the device. These are nano–microscale geometrical features that interact with the waveguided and plasmonic modes in a way that directs them outwards to the viewing direction. These features are usually periodic in nature and have dimensions on the order of a wavelength in both size and pitch. Varying the geometry of the device layers and their interfaces effectively outcouples light by limiting total internal reflection. Nanopixel arrays and other periodic EML nanostructures were shown by Marcato *et al.* (2025) to control the direction and polarization of emitted light. The findings highlight that photonic structuring of the device geometry is as critical to performance as the development of the constituent organic semiconductor materials. [27]

To measure the EQE of an OLED, we determine the number of outcoupled photons and injected electrons with a measurement setup and mathematical methods. The root equation for determining device EQE is:

$$EQE = \frac{N_p}{N_e} \tag{1}$$

where N_p is the number of outcoupled photons and N_e is the number of injected electrons. Determining the number of injected electrons is simply given by:

$$N_e = I_{OLED}/q \tag{2}$$

where I_{OLED} is the current flowing through the OLED and q is the elementary charge, with the value of $1.602 \cdot 10^{-19}\ Coulombs$. Determining the number of photons emitted into free air is more complicated, because the measurement is affected by multiple factors. First, counting the number of photons is always an indirect measurement; photons themselves cannot be counted, but their energy can be captured by devices that convert it into a measurable current. This is achieved by a photodiode, where the energy of a photon is used to excite an electron into a conducting state in a semiconductor material. Second, there are optical losses; not all light that is emitted from the device can be collected in the first place. If a large-area photodiode is placed in front of the emitting device, all light incident at any angle against the photodiode surface normal will experience reflection losses, which grow as the incidence angle increases. Third, a photodiode has a wavelength dependent responsivity; the efficiency of energy conversion in a photodiode is not perfect and varies with wavelength of light. Similarly, an OLED is a broadband emitter, meaning that the range of wavelengths output by the device is relatively large. Different wavelengths equal different quanta of energies. Furthermore, the emission intensity is inherently angle-dependent, while the spectral profile can also vary with viewing angle in devices with strong microcavity effects: devices that incorporate microcavities experience a blueshift at increased viewing angles. Figure 7 describes the angle-dependency of OLED spectral effects.

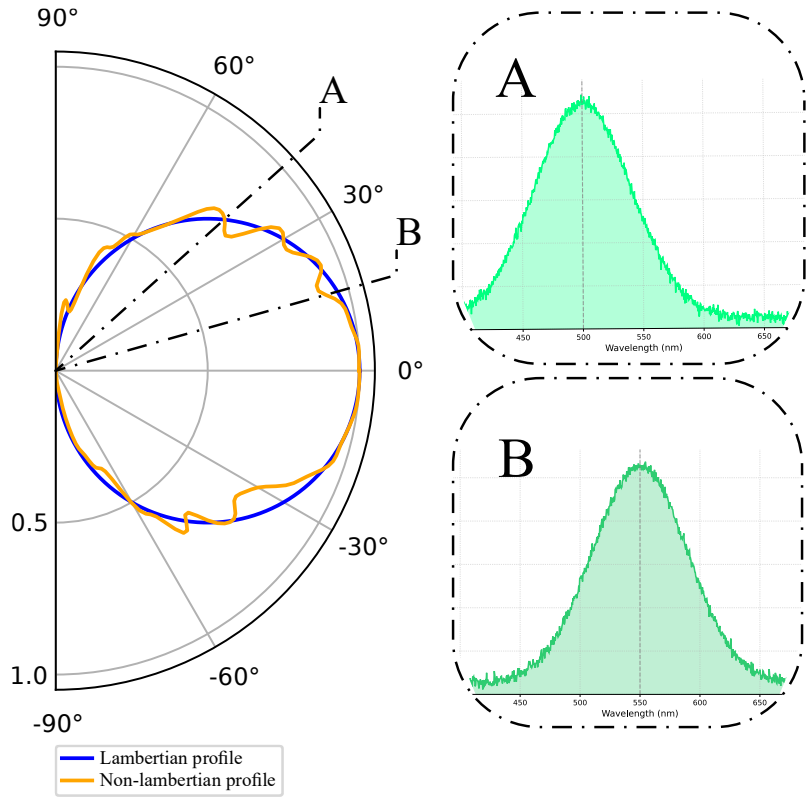

Figure 7. Qualitative graph of the angle dependence of spectral emission from an OLED. The polar plot shows normalized intensities of 2 types of emitters: a Lambertian and a non-Lambertian one. A Lambertian emitter is one of perfect diffuse emission: the emission is of constant radiance, meaning that the measured intensity decreases purely because a smaller projected area of the emitter is viewed. Accordingly, a non-Lambertian emitter—which an OLED typically is—deviates from this. The output wavelength spectrum may also change with the viewing angle: a blueshift is typically observed for microcavity OLEDs. This is presented in subplots A and B. An assumption of Lambertian emission and constant spectrum when calculating device efficiency will lead to an over- or underestimate.

Because not all light can be collected without using an integrating sphere, the following setup is used: a photodiode is placed at a distance from the emitter, such that the incident light is normal to the photodiode. The solid angle subtended by the photodiode in relation to the emitter is calculated, and this information together with previously discussed factors are used to mathematically calculate the number of outcoupled photons.

The full mathematical formulation of the device efficiency is as follows: we first calculate the angle-dependent spectral 'shape' correction factor with equations 3 and 4:

$$F_e(\theta) = \frac{\int S(\lambda,\theta)\lambda d\lambda}{\int S(\lambda,0)\lambda d\lambda} \tag{3}$$

$$C_s = 2\pi \int F_e(\theta)\sin(\theta)\, d\theta \tag{4}$$

where $F_e(\theta)$ is the spectral correction factor as a function of angle (θ), and C_s is the full shape correction including spherical geometry. $S(\lambda, \theta)$ and $S(\lambda, 0)$ represent spectral intensity measured at the changing angle θ and at normal incidence, respectively. Both the numerator and denominator are multiplied by λ/hc—where h is Planck's constant and c is the speed of light—to yield a relative photon count[2].

The photodiode responsivity correction factor is given by:

$$C_{pd} = \frac{\int S(\lambda, 0)\lambda d\lambda}{\int S(\lambda, 0)R(\lambda)d\lambda} \tag{5}$$

where the variables are the same as in equation 3, but with the addition of photodiode responsivity $R(\lambda)$. This correction factor shows how much relative current is generated from a measurement made at normal incidence. The resultant units for C_{pd} are $J \cdot m/Coulombs$. For this equation there is no angle dependence, because the final power measurement is only done at $\theta = 0$.

The average energy of a photon at normal incidence is given by:

$$E_{ph} = hc \cdot \frac{\int S(\lambda, 0)d\lambda}{\int S(\lambda, 0)\lambda d\lambda} \tag{6}$$

where the variables are the same as in the equations before. Equation 6 essentially shows the total measured power divided by the total number of received photons at $\theta = 0$.

The number of photons is therefore found with:

$$N_p = \frac{I_0}{E_{ph}} \cdot C_s \tag{7}$$

where I_0 is the radiant intensity at $\theta = 0$, measured from photodiode current.

Combining and substituting equations 1–7 yields the EQE as percentage:

$$\eta_{EQE} = 100 \cdot \frac{1}{hc} \cdot \frac{r^2}{A_{pd}} \cdot \frac{I_{pd} \cdot q}{I_{OLED}} \cdot C_{pd} \cdot C_s \tag{8}$$

[2] Photon count $\propto Energy \cdot \lambda$

where r is the distance from the light source to the photodiode, A_{pd} is the area of the photodiode, I_{pd} is the measured photodiode current, q is the unit charge and I_{OLED} is the measured current at the OLED device. The given formulation strictly requires that the measurements are taken exactly as intended, otherwise the resulting EQE value will be false. The equations and discussion presented here are based on [28,29].

Since OLEDs do not emit light evenly in all directions, measuring them from just one angle yields a false efficiency value. We need to measure the full angular distribution to get accurate estimates. Section 3 explains the design and fabrication of the machine built for this purpose.

3 Designing a goniometric device for emission characterization

For optics and spectroscopy laboratories, ready-made products for specific tasks are rarely available off-the-shelf. Instead, companies offer standard optomechanical products that are then arranged by the scientist to the exact configuration needed to achieve their goals. These configurations are rarely able to be transferred off the optics workbench, use a relatively large amount of space, and they are suboptimal in achieving the wanted results. In this work, these limitations are overcome with a purpose-built goniometric emission characterization setup. Additionally, a novel OLED sample holding and temporary encapsulation design is presented. A full textual description of every employed design feature is omitted, since these mostly benefit from a graphical representation. These technical drawings are found in the appendices as supplementary figures.

3.1 Design philosophy and methodology

The primary constraint in any design decision made during the project was the goal of a device that's fabricable with a polymer extrusion 3D-printer and a set of basic hand tools. The assembly process should be simple enough for any scientist—skilled in handcraft or not—to do in an afternoon when the standard or vendor parts have been procured and the others fabricated.

The methodology in the first stages of design was loosely based on Axiomatic Design theory (AD) by Suh [30]. AD is based on 2 fundamental axioms: the independence axiom and the information axiom. The independence axiom tells us that each design solution should only map to its corresponding functional requirement. This allows for an uncoupled design that is easy to change and manage. The information axiom tells us that the design that contains the least amount of information is the best design—or effectively the simplest way all the functional requirements can be met.

After initially defining the key functions of the device, a rapid prototyping approach was adopted: incremental design changes were made to each subassembly and component, and the effects were tested by fabricating prototype parts and assemblies. This method yielded a tacit understanding in what works and what does not and allowed quick decision making in what ideas should be abandoned, rethought or continued.

3.2 Mechanical design

The measurement system utilizes a goniometric scheme to enable angle-resolved measurement. This configuration allows for independent control of excitation and detection angles in Photoluminescence (PL) mode, while varying only the viewing angle for Electroluminescence (EL). The kinematic arrangement was chosen such that the sample and a single arm rotate about a central axis, while another stationary arm is set to statically point towards the sample. Figure 8 displays a schematic of the designed kinematic solution, and the final design is presented in Supplementary Figure 1.

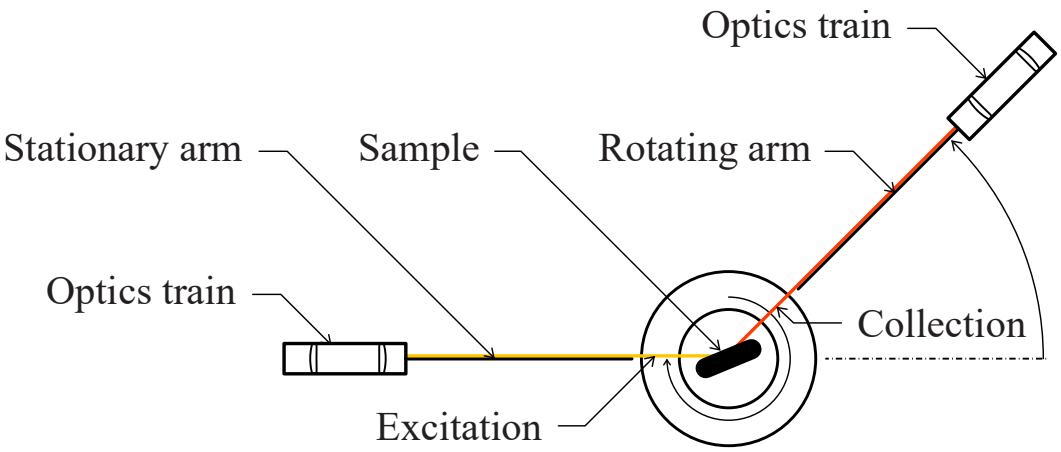

Figure 8. Schematic of the kinematic solution. The sample is situated at the center of rotation; the sample can be rotated 360 degrees in both directions, while the rotating arm can be rotated around the sample at an arc limited by the stationary arm, in both directions.

The goniometric setup presented here is the basis for gathering the spectral data needed to calculate the shape correction factor (equations 3 & 4).

The kinematic concept stayed unchanged throughout the project but went through several iterations of design. After encountering a multitude of problems including lack of rigidity, bad positional accuracy due to tolerance stacking, and fit and assembly problems, a final design was accomplished that solved them all.

As the arms have considerable length, the arising bending moment creates deflection that makes optical alignment and stability a challenge. To ensure rigidity, the cantilevered sections use oversized linear shafts secured via transition fits within the 3D-printed frame. The main rotating shaft is supported by a dual deep-groove ball bearing assembly, which constrains it and minimizes radial runout. For the rotating arm, a similar dual-bearing configuration was used. The bearings employ interference fits; looser fits allow the bearings to sit off axis to one

another, which was observed to cause noticeable deflection of the rotating arm due to precession.

Excessive tolerance stacking was solved by figuring out ways to reduce the total number of parts, and especially interfaces involving 3D-printed parts. Interfaces involving a 3D-printed part and relative motion between the components were eliminated. The dimensions of fits involving 3D-printed parts were solved iteratively, changing compensation offsets until the desired fit was achieved for each part.

The assembly is driven by 2 stepper motors that serve two functions: to independently rotate both the sample and the rotating arm, and to hold one or both components in position. A gear reduction is employed to increase the available torque and angular resolution—a full motor step in the resulting design has a resolution of 0.45 degrees.

Radial runout of the central shaft was measured at 0.05–0.15 mm at approximately 100 mm height. To verify the independence of the rotating components, coupling was inspected by rotating one axis while monitoring the other; observed movement was < 0.01 mm, indicating effective decoupling of the components. Drawings of the full assembly can be seen in Supplementary Figure 4.

3.3 Optics design

The main purpose of the optical system is to map the angle-dependent emission spectra of an OLED sample. Fortunately, this doesn't require an accurate imaging system, which substantially simplifies the optical design; the only requirement is to couple the emitted light into an optical fiber that transports it to a spectrometer. To achieve this requirement, a set of plano-convex lenses are used to collimate the light and focus it into an optical fiber. The lenses are placed in a lens tube that is attached to a 2-axis translation stage which houses the optical fiber and allows to position it accurately. The first iteration of the collection optics design is shown in Figure 9.

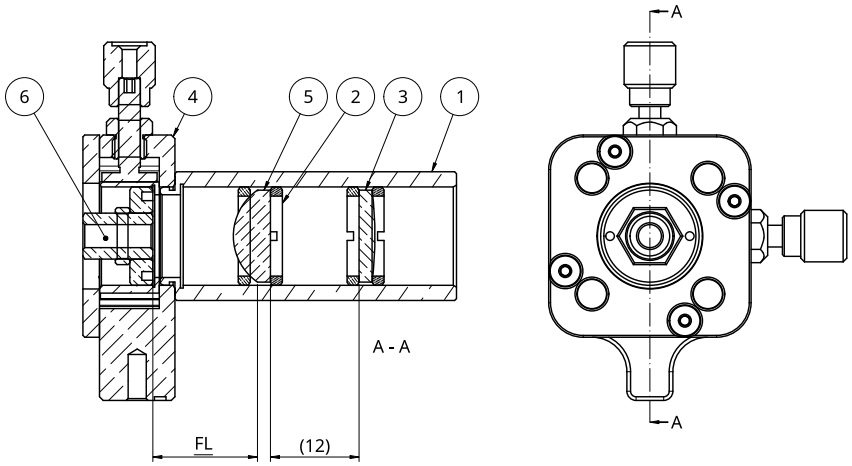

Figure 9. Optical assembly consisting of 1. Lens tube, 2. Retaining rings, 3. 100 mm focal length plano-convex lens, 4. XY-translation stage, 5. 15 mm focal length plano-convex lens, and 6. SMA optical fiber coupler.

The front lens (facing the light source) in the optics train collimates the incoming light, and aides to limit aberrations to shrink the spot diameter achieved by the second lens. The second lens focuses light to the tip of the optical fiber, where the core was initially, in our case, of diameter 600 µm.

The focal length of the front lens was determined by analyzing the collection half-angle against the distance from the source. To yield high spatial resolution, the half-angle should be minimized. This comes with a trade-off of increasingly longer distances for smaller decreases in angle, as visualized in Figure 10.

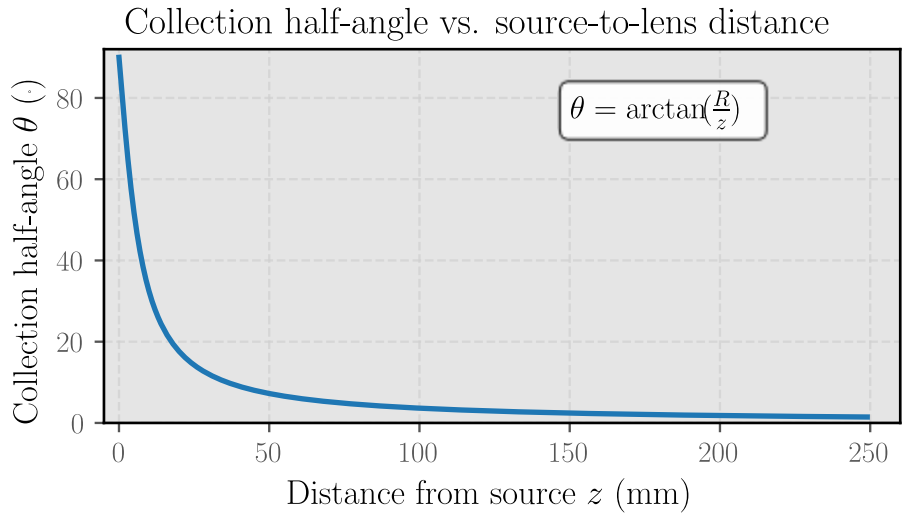

Figure 10. The collection half-angle decreases rapidly until a source-to-lens distance of 50 mm. After 100 mm, the change in angle is no longer meaningful. A focal length of 100 mm for the first lens allows for minimal collection half-angle, while keeping the design compact.

The optical system was further optimized from the initial design: the second lens (balloon 5 in Figure 9) was changed to a lens with a longer focal length of 25 mm. Both lenses in the tube were changed to antireflective coated ones and were reversed such that their convex sides faced each other. These changes reduced the spherical aberrations and reflection losses, which in theory allows incoming light to be focused to a spot < 200 µm in diameter. The optical fiber could then also be changed to a smaller one with a 200 µm core, which better matches the spectrometer slit and allows more light to enter the spectrometer.

The sample OLEDs can have multiple pixels at different vertical positions, which makes it necessary to be able to adjust their position on the optical axis. Many approaches to facilitate precise adjustment were tried, but each failed due to problems with accuracy, stability or usability. At this point it was questioned whether the system needs precise vertical positioning for the sample or not. To verify this, a simple geometric raytracing simulation was done [31]. The results are plotted and discussed in Figure 11. The simulation results affirm the choice of foregoing a precision adjustment system, which further simplified the design.

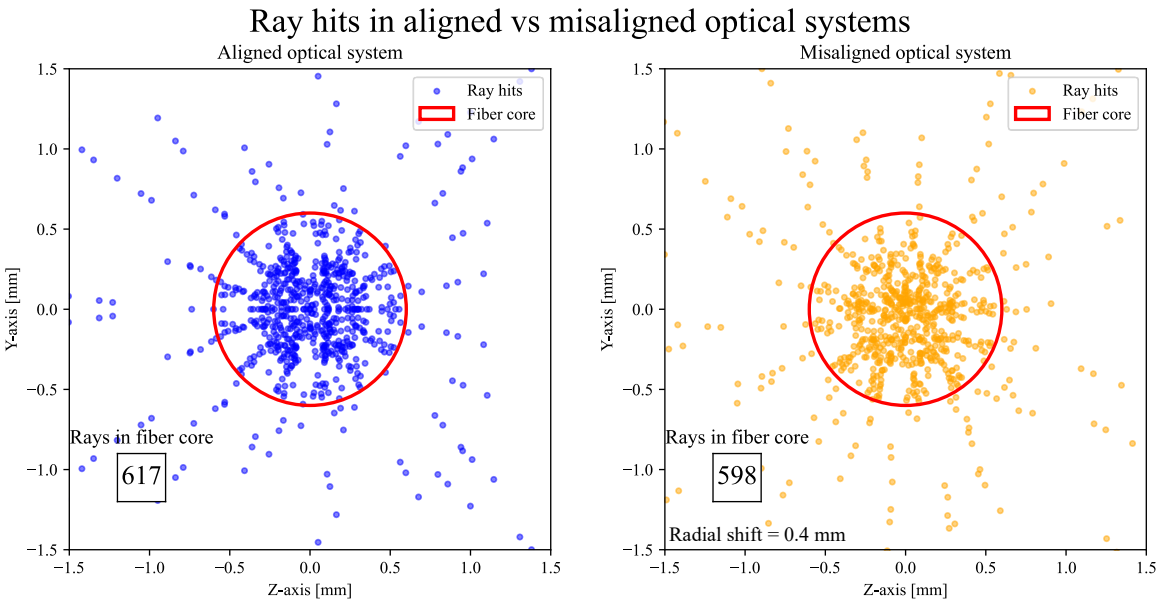

Figure 11. Ray-tracing simulations of the collection optics with a collimating-focusing lens pair. A circle with 600 µm diameter is projected at the center of both plots, representing an optical fiber. Both simulations use the same source, which was set to emit an equal number of 400 nm, 550 nm and 700 nm wavelength rays. For the misaligned simulation, the source was radially shifted 0.4 mm. The result shows that the system is insensitive even to relatively large shifts in emitter position, as ray hits only decreased by 3.1 %.

The optical system is kept symmetric, in that both arms hold mostly the same components; the excitation optics may differ in the choice of lenses based on whether collimated or focused

light is desired. The mechanical design remains identical. Longitudinal optical alignment is facilitated by carrier assemblies attached to linear rails on the goniometer arms. The carrier assemblies hold optical post assemblies with vertical, rotational and tilt adjustment capabilities.

3.4 Sample holder design

The OLED samples that are not hermetically sealed suffer from rapid degradation in an oxygen-rich and moist atmosphere. Experiments conducted with samples like this therefore become time sensitive and less reliable, since the emission characteristics may change between measurements. Furthermore, when the samples degrade, they can no longer be used, and new ones must be fabricated. This is an inefficient use of both time and funds. The present problem necessitates a design for a sample holder which keeps the sample in an inert atmosphere or vacuum, while still allowing for accurate measurement.

In general, it is impossible to stop a gas from diffusing through a barrier when a concentration gradient exists, though certain materials—like glass—perform exceedingly well. OLEDs are effectively protected by encapsulating them with a material like this. The capsules can be glued or welded shut to provide maximal protection. However, the encapsulation method used with experimental devices should allow reopening and changing of the sample, meaning that gluing or welding cannot be done. Furthermore, glove boxes—where the samples are handled—are a suboptimal environment to do these processes. Instead, an additional sealing element is used to interface with the features of the capsule. This seal and the interfaces it creates need to be essentially perfect to stop gases from rapidly exchanging or entering the sealed volume. [11,32]

Sealing OLEDs becomes a challenge, because electricity needs to be fed into the sealed volume, which is done with physical conductors. If these are routed through the sealing interface—even with very thin conductors—an abrupt step is created at the sealing line. The seal cannot conform to this step, as it is not infinitely flexible. Conventionally, this problem could be solved by utilizing vacuum-rated cable feedthroughs. Designs incorporating these were done but ultimately abandoned due to the excessive size and concerns about the ease of use, manufacturability and assembly.

Because of the shortcomings of the conventional feedthrough systems, methods to facilitate the seal were designed and tested. The conductors used for the sample holder are 0.08 mm

thick adhesive-backed copper foil strips. The tested sealing elements were cutouts of a rubber gasket material, and standard O-ring seals. Both elements failed to create a vacuum-tight seal by themselves. The next step was to cover the copper foils in a lacquer to create a smoother transition at the interface cross-section. The efforts here failed, either due to the impossibility of the method or the challenges involved in executing it. Increasing the applied pressure and therefore seal compression also proved futile. What finally worked was applying a layer of vacuum grease—a thick, non-off gassing[3] silicone-based lubricant—on top of the conductors. The grease fills the spaces where the sealing element cannot conform to, creating a vacuum-tight interface.

To verify the function of the sample holder sealing system, a simple oxygen detection system was employed. Anaerobic environment indicator test strips from Sigma-Aldrich were activated and placed in a dummy sample holder consisting of the same conductor strips, O-ring seal and vacuum grease as the real one. Another sealing system was tested for comparison, without the conductors or the vacuum grease. The test strips contain methylene blue: a chemical that changes from transparent to blue upon oxidization. Once water is added on the strip, the methylene blue is reduced into its transparent form. Upon subsequent contact with oxygen, the strip rapidly turns blue to indicate the state of the environment. The test suggested that the internal volume of the sample holder stays relatively oxygen-free for the duration of several days: the strips began changing in color at the sixth day post evacuation, but as they aren't designed for a vacuum environment, the method is not entirely reliable. Figure 12 further explains the sealing system.

[3] Down to $10^{-7}Pa$.

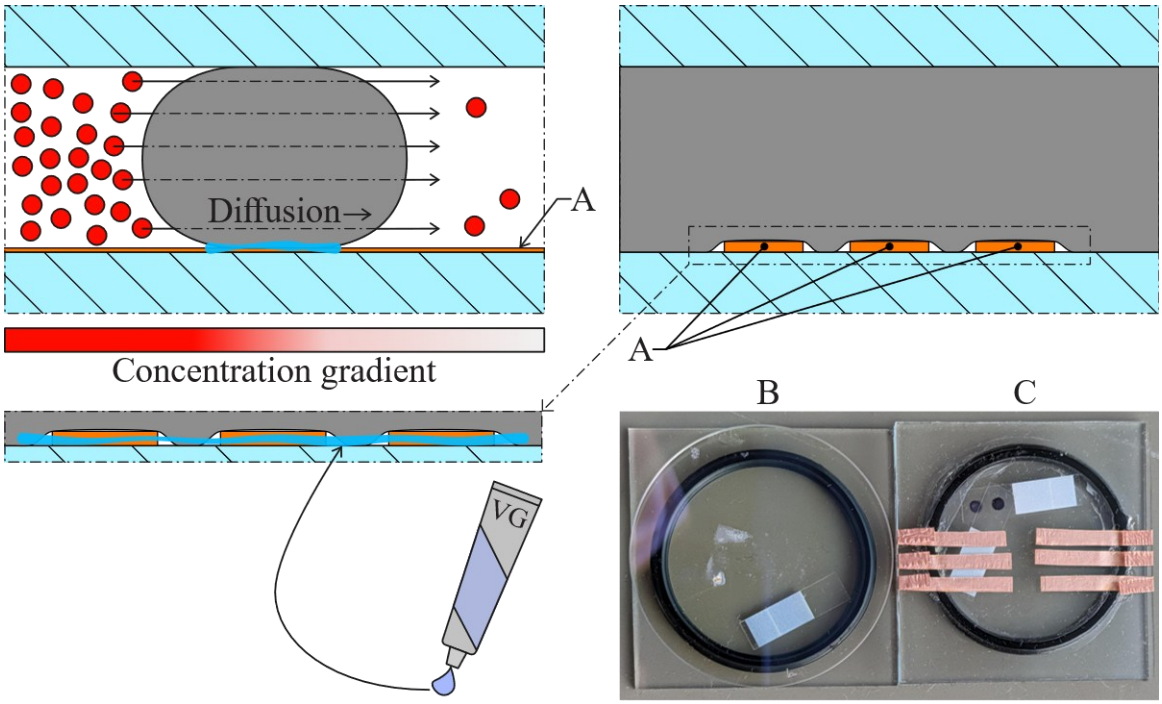

Figure 12. Sample holder sealing system, gas species diffusion and seal testing. *(*A*)* Electrical conductor strip*, (*B*) d*ummy sample holder without conductors or vacuum grease*, and (*C*) d*ummy sample holder with conductors and vacuum grease. Whenever there exists a concentration gradient such that one side of the system has a greater amount (pressure) of a gas species as the other, the system will tend towards equalization even if a physical barrier is in the way. A characteristic feature of such a barrier is its permeability, or susceptibility to molecular diffusion. The diffusion rate depends on the barrier geometry (thickness and surface area), the gas species, the ambient temperature, and the concentration gradient of the gas.
The conducting strips laid under the sealing element partially lift the element up, creating small gaps where gas can freely flow from one side to the other. For this reason, a thin layer of vacuum grease is spread on the interface; its job is to plug the small gaps where the seal fails. The system was tested (subfigures B, C) with oxygen-reactive, color-changing test strips, which indicated that oxygen had certainly entered the sealed volume by day 6, even if the vacuum still held the system closed.

A mathematical verification is done to support the findings, using the engineering form of Fick's first law of diffusion:

$$\mathrm{Q}=\mathrm{K}\cdot\mathrm{A}\cdot\frac{\Delta\mathrm{P}}{\mathrm{s}} \tag{9}$$

where Q is the volumetric flow rate, K is the permeability of the sealing element, A is the area of the sealing element exposed to the diffusing gas, ΔP is the pressure differential of the gas species of interest and s is the thickness of the seal. Plugging in numbers for a 30 mm outer diameter and 3 mm cross-sectional diameter O-ring (simplified to a cylinder) yields [33]:

$$6.5\cdot10^{-8}\frac{cm^3cm}{cm^2s\cdot atm}\cdot 2.83cm^2\frac{0.2atm}{0.3cm}=1.2\cdot10^{-7}cm^3/\mathrm{s} \tag{10}$$

which translates to approximately 0.011 cubic centimeters of oxygen per day, or 1 ml every 100 days in standard conditions.

Working with the OLED samples has revealed that significant degradation happens on the order of an hour in a normal atmosphere, due to the water and oxygen content. Based on this observation and the ongoing discussion, a safe assumption can be made, that the samples will survive at least 24 hours while enclosed in the sample holder, giving ample time to make measurements while also making them more reliable.

The resulting sample holder design consists of 2 pieces of 30x30x2 window glass sheets, a soft 3D-printed TPU cradle with raised contact bosses for the sample, and the electrical conductor strips. Initially, an adhesive was used to attach the cradle in position but this was later found to be redundant since the adhesive-backed conductor strips can hold the cradle on their own. The completed system includes a clamping assembly, which consists of a 3D-printed shell and fasteners for compression. The system is better represented in Supplementary Figure 3.

3.5 Electronics and software

The system electronics are built around an Arduino Nano, which controls motor movement. Power is supplied by a 12 V source to two stepper motor drivers. The central shaft uses an EasyDriver stepper driver, while the rotating arm uses a higher-current DRV8825 to handle the larger load and moment of inertia. To maximize torque, the micro-stepping pins on both drivers were grounded, forcing the motors into full-step operation. Spectral data is collected by an Ocean Optics USB2000 spectrometer, which is triggered directly by the control program.

The control program was configured in LabVIEW to manage both the hardware and data acquisition. The interface allows the user to set scan parameters, including angular limits, step size, and integration time. During a measurement, the software synchronizes the motor movement with the spectrometer and automatically exports the angle-resolved data to a file for post-processing in Python.

4 Experiments and results

Prior to EL characterization, a systematic alignment procedure was developed and performed to define the system's coordinate system. This step is critical to ensure that the sample's axis of rotation is collinear with the collection optics' optical axis, thereby minimizing parallax errors during measurement.

The primary optical axis (shared by the collection and excitation optics) was established using a white-light maximization technique. A tungsten-halogen source was coupled into the excitation arm via an optical fiber, and the beam path was spatially filtered using a dual-aperture lens tube (1.5 mm and 0.5 mm, separated by ~10 mm) to define a collimated reference beam. The collection optics were then iteratively adjusted using a "beam walking" method—optimizing one degree of freedom at a time—until maximum spectral intensity was achieved, confirming that the excitation and collection arms were coaxial.

Once the primary axis was set, the sample holder was installed. After the primary optical axis was established, the 90° position became easy to find: the sample was rotated to approximately 90 degrees, and the intensity was again maximized by sequentially rotating both the arm and the sample one step at a time.

To align the specific OLED pixel with the axis of rotation, the collection optics were first rotated to the surface normal (0°). The white light optical fiber was then temporarily coupled to the collection arm, projecting a focused spot backward onto the sample surface. The sample position was adjusted in-plane until this focal spot coincided with the target pixel. This configuration was chosen over using the standard excitation path because it provided better visibility of the pixel within the measurement environment.

After the whole system was aligned, it was driven to the starting position. A power source was connected to the pixel to be measured and the parameters were set. Measurements were taken from 90 to -60 degrees (geometrically limited angles due to a full 180-degree scan requiring more setup for each run) with 10-degree increments (see Supplementary Figure 6 for a schematic). A total of 25 scans over 2 days were done, out of which the first 6 failed due to problems with either hardware or software; only the successful measurements are presented. The power source was manually pulsed—turned off between exposures—due to no software implementation at the time. The results are presented in Figure 13.

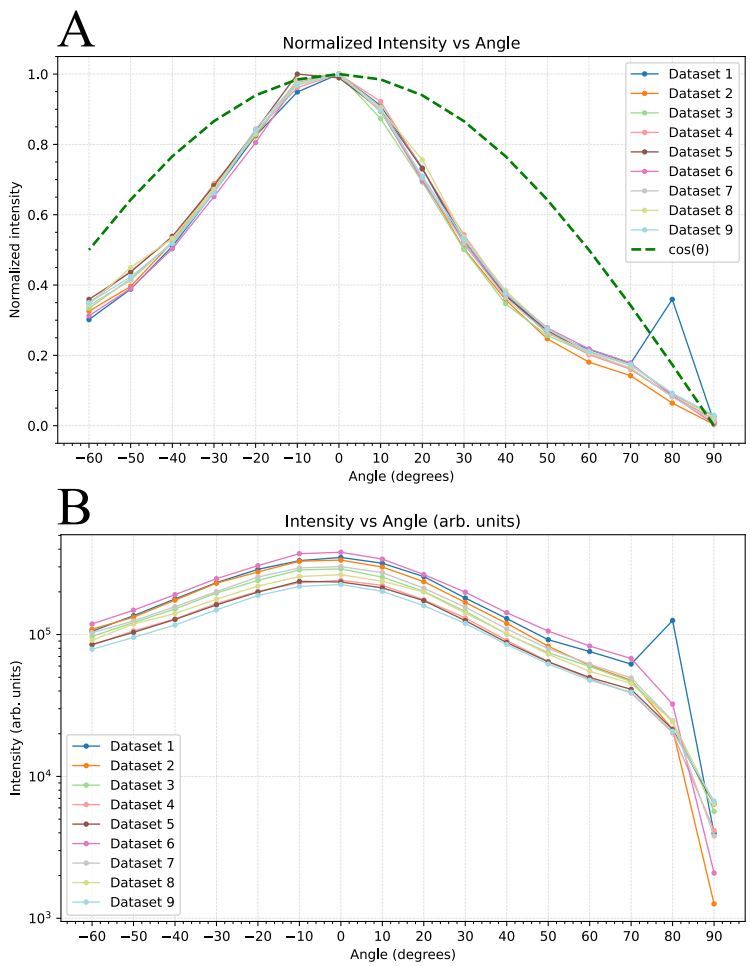

Sample: MM237
I = 150 µA
V_{max} = 12 V

Dates and times

Dataset 1	2026-02-05	15:11
Dataset 2	2026-02-05	16:28
Dataset 3	2026-02-05	16:32
Dataset 4	2026-02-05	16:36
Dataset 5	2026-02-05	16:42
Dataset 6	2026-02-06	8:48
Dataset 7	2026-02-06	8:52
Dataset 8	2026-02-06	8:55
Dataset 9	2026-02-06	9:00

Figure 13. Results of EL measurements of a blue OLED. (A) Angle-resolved normalized intensity; at each angle, the whole measured spectrum is integrated. The result is normalized against the 0-angle value for each scan. This yields the shape factor (equations 3 & 4). The Lambertian cosine function is plotted as reference. (B) Logarithmic plot of the measured and integrated spectral intensities (arbitrary units). The plot shows the degradation between measurements that happens as the sample is electrically excited. (C) Photograph of the sample and the measured pixel: from the onset, the pixel was degraded.

As can be seen from Figure 13 A, the emission follows a sub-Lambertian distribution. If the EQE of the OLED was to be determined using a photocurrent measurement at normal incidence and a Lambertian assumption, the result would be an overestimate, which highlights the need for angle-resolved characterization.

Datasets 1–9 were gathered over 19 hours on different days, with no further degradation of the OLED—conversely, the first measurement taken on the second day yielded an increase in intensity of 8.73 %, suggesting that some form of regeneration had happened. The intensity then rapidly decreased to the level of the last measurements taken on the previous day, and continued to decline steadily as the sample was excited. Table 2 displays the relative change in intensities compared to the first measurement.

Table 2. Change in maximum intensity between measurements on days 1 and 2.

Dataset	Intensity change (over first measurement)	
1	0 %	Day 1
2	-4.22 %	
3	-16.87 %	
4	-31.04 %	
5	-32.88 %	
6	+8.73 %	Day 2
7	-13.80 %	
8	-24.50 %	
9	-35.56 %	
10	-35.38 %	
11	-47.29 %	
12	-54.04 %	
13	-52.60 %	
14	-54.83 %	
15	-56.61 %	
16	-57.99 %	
17	-57.25 %	
18	-58.03 %	
19	-58.01 %	

The sample was kept enclosed for a total of 28 days, throughout which it was luminous when excited with the same maximum driving voltage as on day 1. The intensity measured on the last day was approximately a third of the initial; at this point, over 50 measurement runs were done. The sample was then released from the enclosure—subjected to ambient air—and was verified to be functioning. On the next day, the sample was dead. This, together with the experimentation discussed in section 3.4, implies that the sample holder design effectively shields the sample from environmental degradation.

The non-axially symmetric distribution shown in Figure 13 was first attributed to the degradation of the pixel, but it was later discovered that the method used to align the pixel was the cause: because the alignment light source and the spectrometer used different optical fibers, the projected alignment spot did not match with the collection spot. The method is still useful to get the alignment close, but final alignment is achieved by adjusting the sample position to match the measured intensity at -45 and 45 degrees. This method was used for a new sample, and the data showed better axial symmetry, and is displayed in Figure 14.

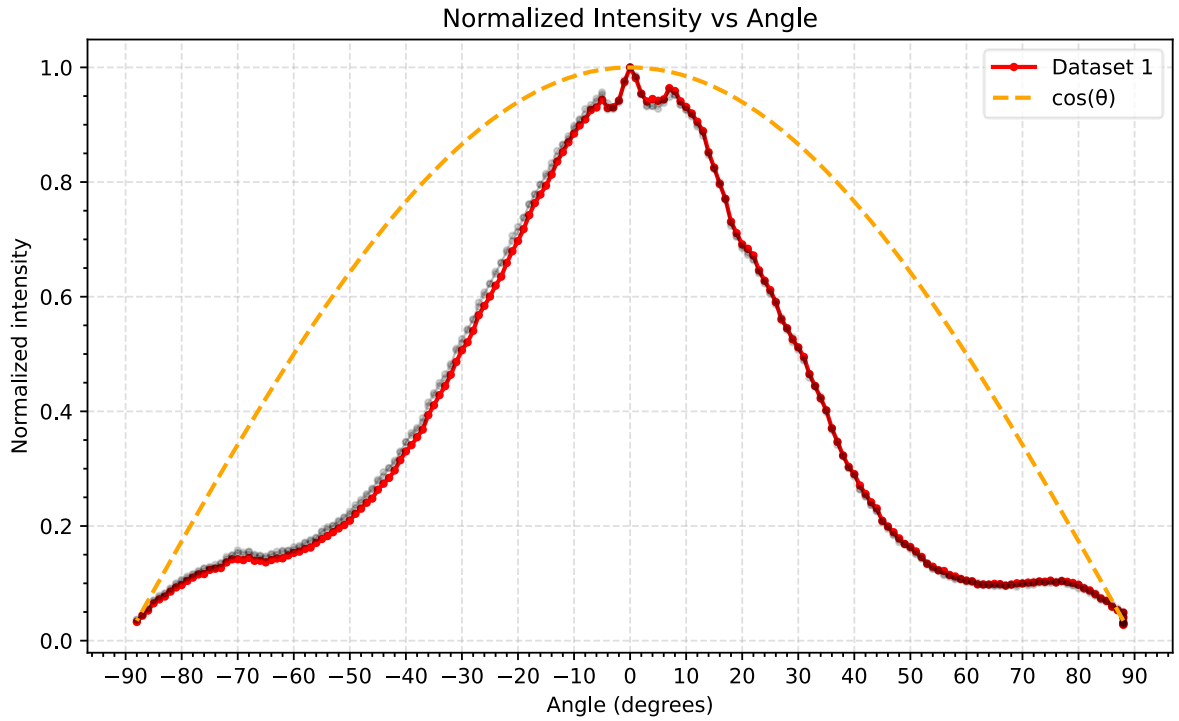

Figure 14. Normalized intensity plot of a new sample and better alignment, from 88 to -88 degrees.

The shape correction factor was calculated for the new sample, per equations 3–4. To smooth the remaining errors in alignment, the correction factor was calculated for both negative and positive angles (using the absolute value for the negatives) and then averaged. The missing 2 degrees on each side can be left unaccounted for, since their contribution is negligible as the intensity here is essentially 0. The calculated shape correction factor is approximately 1.72; compared to the factor of ~3.14 for a true Lambertian emitter, the difference is approximately 45 %. If the EQE was to be calculated using a photocurrent measurement at normal incidence and a Lambertian assumption, the result would be a great overestimate.

5 Conclusions

The drive for higher-efficiency light emitting devices necessitates the development of precise characterization tools that allow simple, reliable and accurate operation. While OLEDs provide practically limitless customization in terms of both emission characteristics and device form factor, they represent key measurement challenges: OLEDs rarely display an emission distribution that follows one of a perfect Lambertian, and might experience microcavity-related, viewing angle dependent spectral effects. OLEDs are also left vulnerable to the outside environment; the reliability of any measurement is compromised whenever a sample is taken out of an inert atmosphere. These challenges are addressed by this thesis through the design, fabrication and validation of a low-cost goniometric measurement system and an inert-atmosphere sample holder.

The main contribution of this work is the development of a goniometric system capable of semicircular spectroscopic measurements with half-degree resolution. By utilizing a kinematic design with independent rotation for the sample and the collection arm, the system achieves the mechanical flexibility required for Electroluminescence (EL), Photoluminescence (PL), and reflectivity measurements. The design philosophy of accessibility was successfully realized; the device relies almost entirely on vendor-sourced components and 3D-printed parts, making it easily reproducible for other research groups.

The developed sample holder addresses the issue of environmental degradation. While a statistical lifetime study was outside the scope of this work, the design was validated through two complementary methods. First, chemical indicator tests demonstrated that the sealing mechanism maintains an oxygen-free environment for up to six days. Second, the functional OLED test showed that the sample remained viable for measurement for over 18 hours—and functional for almost 4 weeks—which is a significant improvement over the typical survival time of unencapsulated devices in ambient air.

The system was validated through EL characterization of an OLED sample. A protocol for sample preparation and initial optical alignment was detailed, and multiple spectral scans were successfully done. The results show a sub-Lambertian intensity distribution, confirming that relying on standard Lambertian assumptions when characterizing devices like these will lead to inaccurate results. A shape correction factor of approximately 1.7 was determined for the measured OLED based on the measured data.

Future work regarding the present system consists of optimization or redesign of the goniometer system, and possible improvements in the sample holder design. The electronics design should be revised: as it stands, the choice of components is suboptimal. Better motor drivers, more powerful motors and possibly another microcontroller should be considered. The LabView program that runs the system requires further optimization in terms of logic, bug fixing and system automaticity, since the system remains very manual in its operation.

Procedures for making EL, PL and reflectivity measurements need to be developed and documented. Fresh OLED samples should be fabricated and characterized, and the data should be used to calculate the device EQEs and then compare the results to a known reference—such as a measurement done in an integrating sphere.

In conclusion, this thesis showed that angle-resolved characterization of OLEDs is achievable with a cost-effective, custom-built solution. The present work contributes a valuable tool to the ongoing development of efficient lighting and display technologies.

References

[1] Commission Delegated Regulation (EU) 2019/2013 of 11 March 2019 supplementing Regulation (EU) 2017/1369 of the European Parliament and of the Council with regard to energy labelling of electronic displays and repealing Commission Delegated Regulation (EU) No 1062/2010 (Text with EEA relevance)Text with EEA relevance, 2021. http://data.europa.eu/eli/reg_del/2019/2013/2021-05-01 (accessed February 10, 2026).

[2] Electronic Displays - European Commission, (n.d.). https://energy-efficient-products.ec.europa.eu/product-list/electronic-displays_en (accessed February 14, 2026).

[3] N. Holonyak Jr., S.F. Bevacqua, COHERENT (VISIBLE) LIGHT EMISSION FROM Ga(As1−xPx) JUNCTIONS, Appl. Phys. Lett. 1 (1962) 82–83. https://doi.org/10.1063/1.1753706.

[4] C.W. Tang, S.A. VanSlyke, Organic electroluminescent diodes, Applied Physics Letters 51 (1987) 913–915. https://doi.org/10.1063/1.98799.

[5] C. Kang, M.F. Prodanov, J. Song, K. Mallem, Z. Liao, V.V. Vashchenko, A.K. Srivastava, Robust, Narrow-Band Nanorods LEDs with Luminous Efficacy > 200 lm/W: Next-Generation of Efficient Solid-State Lighting, Small 20 (2024) 2311671. https://doi.org/10.1002/smll.202311671.

[6] Targeting 100% LED lighting sales by 2025 – Analysis, IEA (2022). https://www.iea.org/reports/targeting-100-led-lighting-sales-by-2025 (accessed August 6, 2025).

[7] Light Sources - European Commission, (n.d.). https://energy-efficient-products.ec.europa.eu/product-list/light-sources_en (accessed February 14, 2026).

[8] Energy Conservation Program: Energy Conservation Standards for General Service Lamps, Federal Register (2024). https://www.federalregister.gov/documents/2024/04/19/2024-07831/energy-conservation-program-energy-conservation-standards-for-general-service-lamps (accessed February 14, 2026).

[9] IKEA Vitsand OLED | OLED-Info, (n.d.). https://www.oled-info.com/ikea-vitsand-oled (accessed November 5, 2025).

[10] LG Chem Launches New 406x50mm Flexible OLED Light Panel, LED Professional - LED Lighting Technology, Application Magazine (n.d.). https://www.led-professional.com/products/leds_led_modules/lg-chem-launches-new-406x50mm-flexible-oled-light-panel (accessed November 5, 2025).

[11] R. Liguori, F. Nunziata, S. Aprano, M.G. Maglione, Overcoming Challenges in OLED Technology for Lighting Solutions, Electronics 13 (2024) 1299. https://doi.org/10.3390/electronics13071299.

[12] What Are Folding Phone Screens - HONOR SA, (n.d.). https://www.honor.com/sa-en/blog/what-is-a-foldable-phone/ (accessed February 12, 2026).

[13] LCD vs. OLED Displays: A Comprehensive Comparison of Performance, Longevity, and Cost, Riverdi (2023). https://riverdi.com/blog/lcd-display-vs-oled-which-is-better-and-why (accessed February 12, 2026).

[14] W.D. Callister, D.G. Rethwisch, Electrical properties of selected materials, in: Materials Science and Engineering: An Introduction, 10th Edition, n.d.: pp. 696, 700, 719.

[15] R.A. Matula, Electrical resistivity of copper, gold, palladium and silver, 1979. https://srd.nist.gov/JPCRD/jpcrd155.pdf (accessed July 20, 2025).

[16] Dong Wook Shin, M. Tomozawa, Electrical resistivity of silica glasses, Journal of Non-Crystalline Solids 163 (1993) 203–210. https://doi.org/10.1016/0022-3093(93)90769-t.

[17] Energy bands, in: Elementary Semiconductor Device Physics: Understanding Energy Band Formation Using Circuit Theory, 1st ed., CRC Press, Boca Raton, 2024. https://doi.org/10.1201/9781003439417.

[18] W.D. Callister, D.G. Rethwisch, Energy band structures, in: Materials Science and Engineering: An Introduction, 10th Edition, n.d.: pp. 691–695.

[19] S.R. Forrest, Organic Electronics: Foundations to Applications, 1st ed., Oxford University PressOxford, 2020. https://doi.org/10.1093/oso/9780198529729.001.0001.

[20] M.E. Abdelhamid, A.P. O'Mullane, G.A. Snook, Storing energy in plastics: a review on conducting polymers & their role in electrochemical energy storage, RSC Adv. 5 (2015) 11611–11626. https://doi.org/10.1039/c4ra15947k.

[21] G. Huseynova, Inorganic versus organic semiconductors, MSEIJ 4 (2020). https://doi.org/10.15406/mseij.2020.04.00145.
[22] M.D. Hanwell, D.E. Curtis, D.C. Lonie, T. Vandermeersch, E. Zurek, G.R. Hutchison, Avogadro: an advanced semantic chemical editor, visualization, and analysis platform, J Cheminform 4 (2012) 17. https://doi.org/10.1186/1758-2946-4-17.
[23] D.G.A. Smith, L.A. Burns, A.C. Simmonett, R.M. Parrish, M.C. Schieber, R. Galvelis, P. Kraus, H. Kruse, R.D. Remigio, A. Alenaizan, A.M. James, S. Lehtola, J.P. Misiewicz, M. Scheurer, R.A. Shaw, J.B. Schriber, Y. Xie, Z.L. Glick, D.A. Sirianni, J.S. O'Brien, J.M. Waldrop, A. Kumar, E.G. Hohenstein, B.P. Pritchard, B.R. Brooks, H.F.S. Iii, A. Yu, K. Patkowski, A.E.D. Iii, U. Bozkaya, R.A. King, J.M. Turney, T.D. Crawford, C.D. Sherrill, Psi4 1.4: Open-Source Software for High-Throughput Quantum Chemistry, (n.d.).
[24] A.G. Abdelmagid, Strong Light-Matter Interaction for Efficient Organic Optoelectronics, University of Turku, 2025.
[25] E.V. Puttock, J. Haug, E. Zysman-Colman, S. Bräse, Hyperphosphorescent OLEDs: Harnessing the Power of MR-TADF Terminal Emitters, Advanced Optical Materials 13 (2025) 2500514. https://doi.org/10.1002/adom.202500514.
[26] K.T. Kamtekar, A.P. Monkman, M.R. Bryce, Recent Advances in White Organic Light-Emitting Materials and Devices (WOLEDs), Advanced Materials 22 (2010) 572–582. https://doi.org/10.1002/adma.200902148.
[27] T. Marcato, J. Oh, Z.-H. Lin, T. Tian, A. Gogoi, S.B. Shivarudraiah, S. Kumar, A. Govind Rajan, S. Zeng, C.-J. Shih, Scalable nanopatterning of organic light-emitting diodes beyond the diffraction limit, Nat. Photon. (2025). https://doi.org/10.1038/s41566-025-01785-z.
[28] E. Archer, S. Hillebrandt, C. Keum, C. Murawski, J. Murawski, F. Tenopala-Carmona, M.C. Gather, Accurate Efficiency Measurements of Organic Light-Emitting Diodes via Angle-Resolved Spectroscopy, Advanced Optical Materials 9 (2021) 2000838. https://doi.org/10.1002/adom.202000838.
[29] P. Cusumano, G. Garraffa, S. Stivala, A simple method for the photometric characterization of organic light-emitting diodes, Solid-State Electronics 195 (2022) 108394. https://doi.org/10.1016/j.sse.2022.108394.
[30] N.P. Suh, Axiomatic Design: Advances and Applications, 2001.
[31] C. Bergmann, Optics Workbench, (2025). https://github.com/chbergmann/OpticsWorkbench (accessed December 18, 2025).
[32] K. Jousten, C.B. Nakhosteen, Handbook of Vacuum Technology, John Wiley & Sons, Incorporated, Newark, GERMANY, 2016. http://ebookcentral.proquest.com/lib/kutu/detail.action?docID=4558132 (accessed February 15, 2026).
[33] Apple Rubber, The Permeability of Rubber Compounds, Hot Topics (2018). https://www.applerubber.com/hot-topics-for-engineers/the-permeability-of-rubber-compounds/ (accessed January 9, 2026).

Appendices

Appendix 1: Supplementary figures

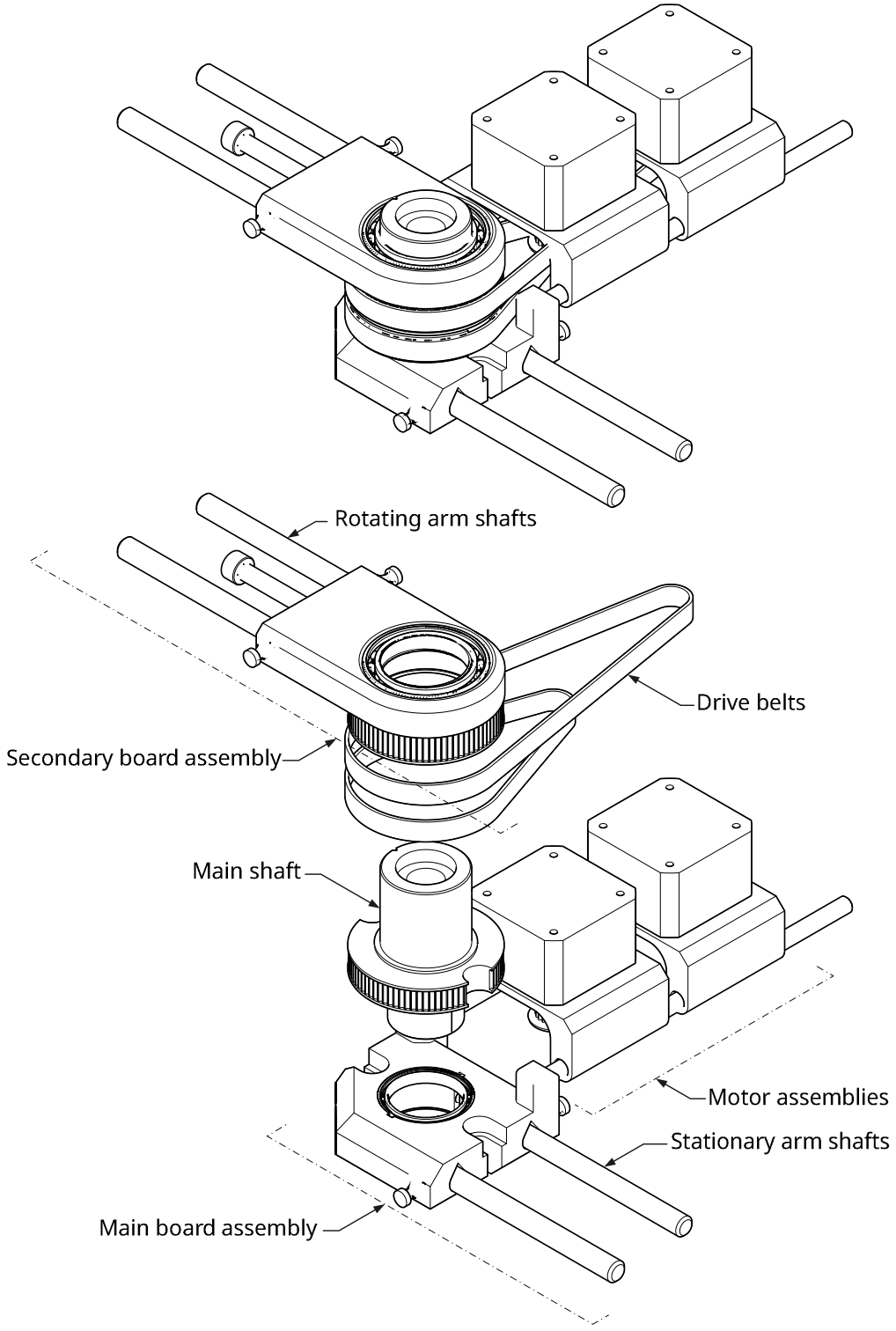

Supplementary Figure 1. Kinematics design. The main board connects the main shaft, motor assemblies and the secondary board. The main shaft and secondary board are uncoupled and can be individually rotated.

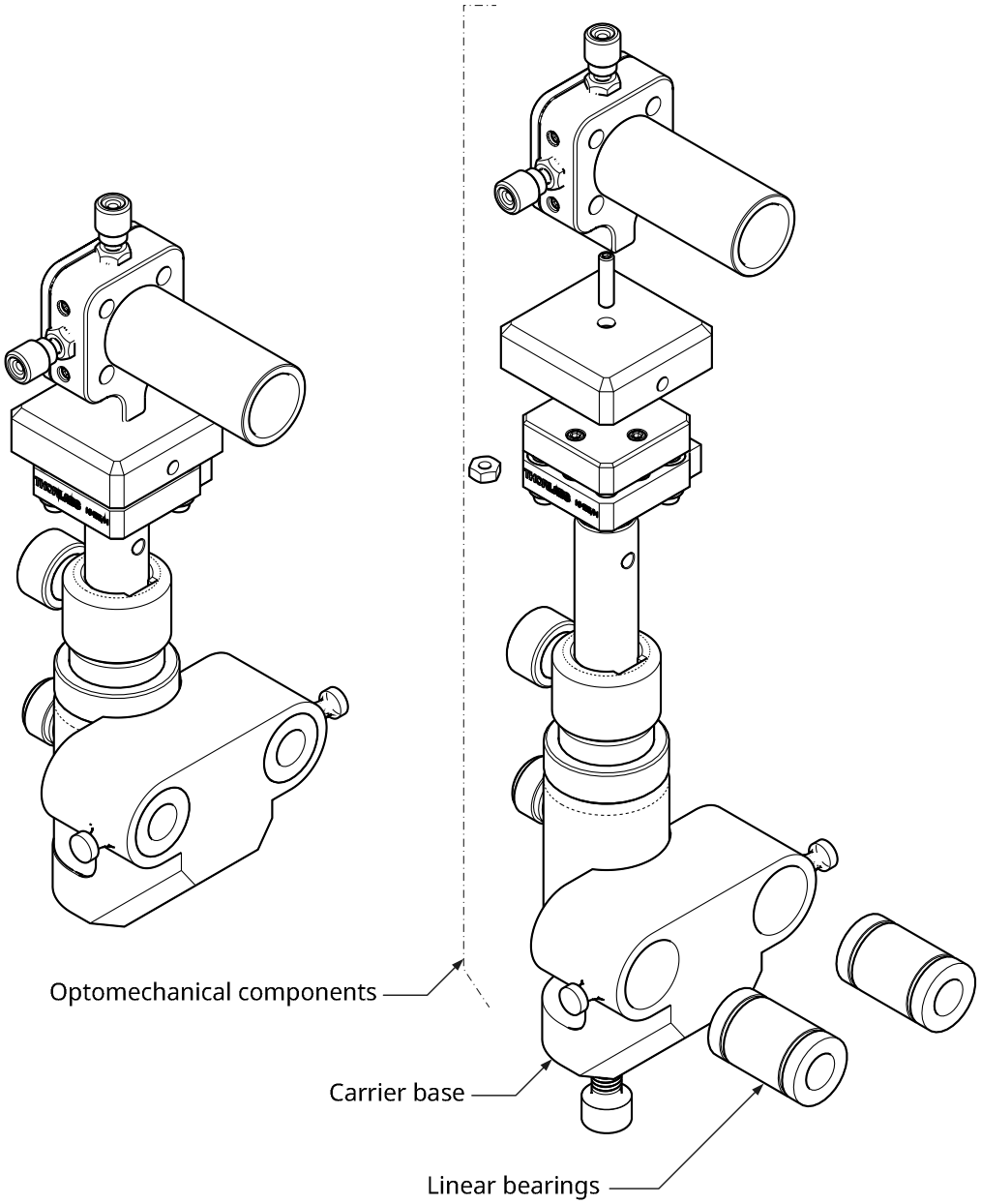

Supplementary Figure 2. Optics carrier assembly. The assembly consists of a base, linear bearings and optomechanical components. The optomechanical components allow vertical and rotational degrees of freedom.

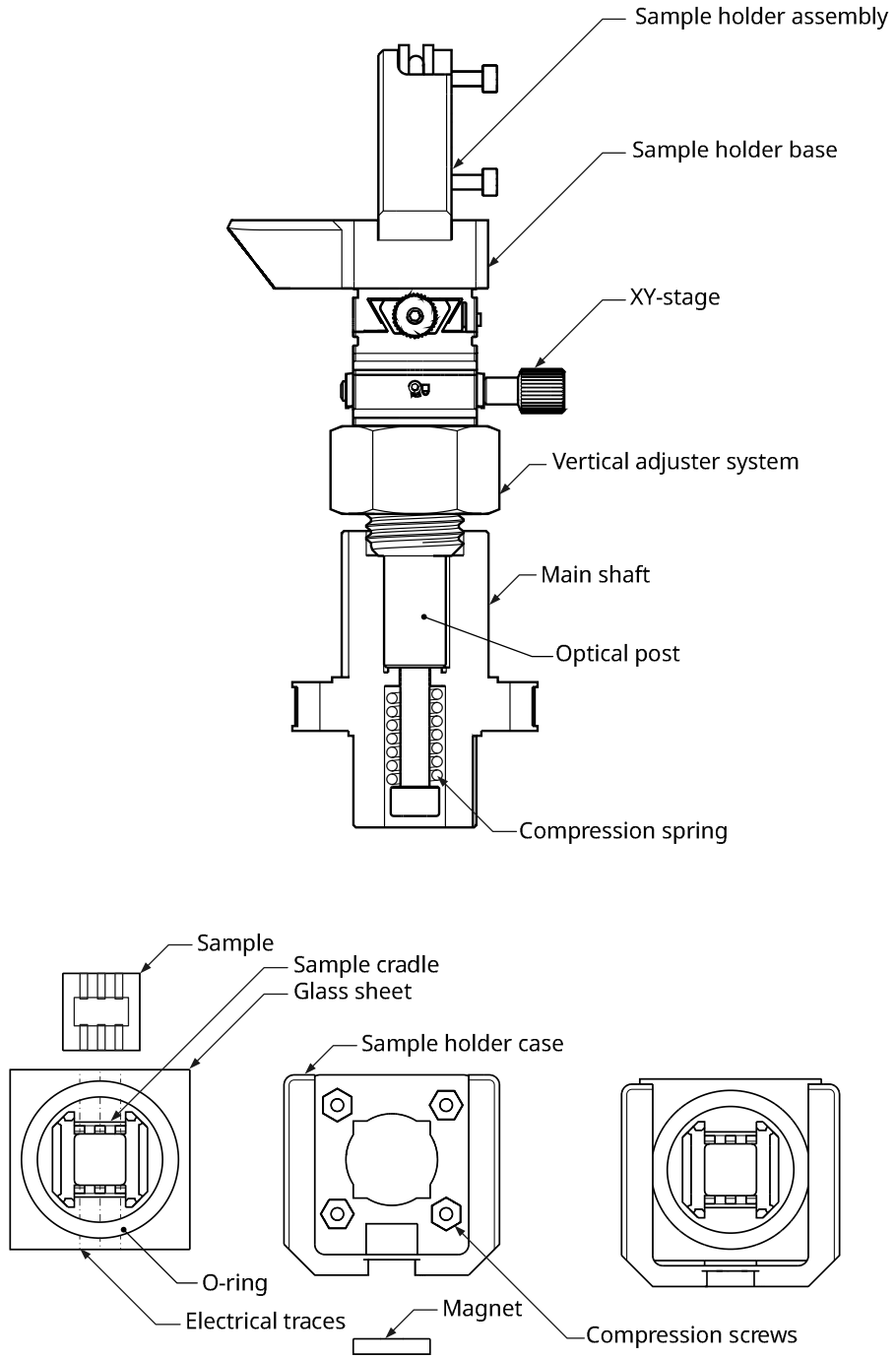

Supplementary Figure 3. Sample positioning system and sample holder. The optical post sits in a cutout in the main shaft. A screw is fastened to a thread in its bottom, and a compression spring is used to exert a force downwards. The post goes through an M20 threaded tube, and on top of the post an XY-stage is fastened. Rotating the adjuster nut forces the assembly to move upwards, while the downward force from the spring removes backlash. The sample holder assembly is held in place by a slot in the sample holder base and contact between their two respective magnets.

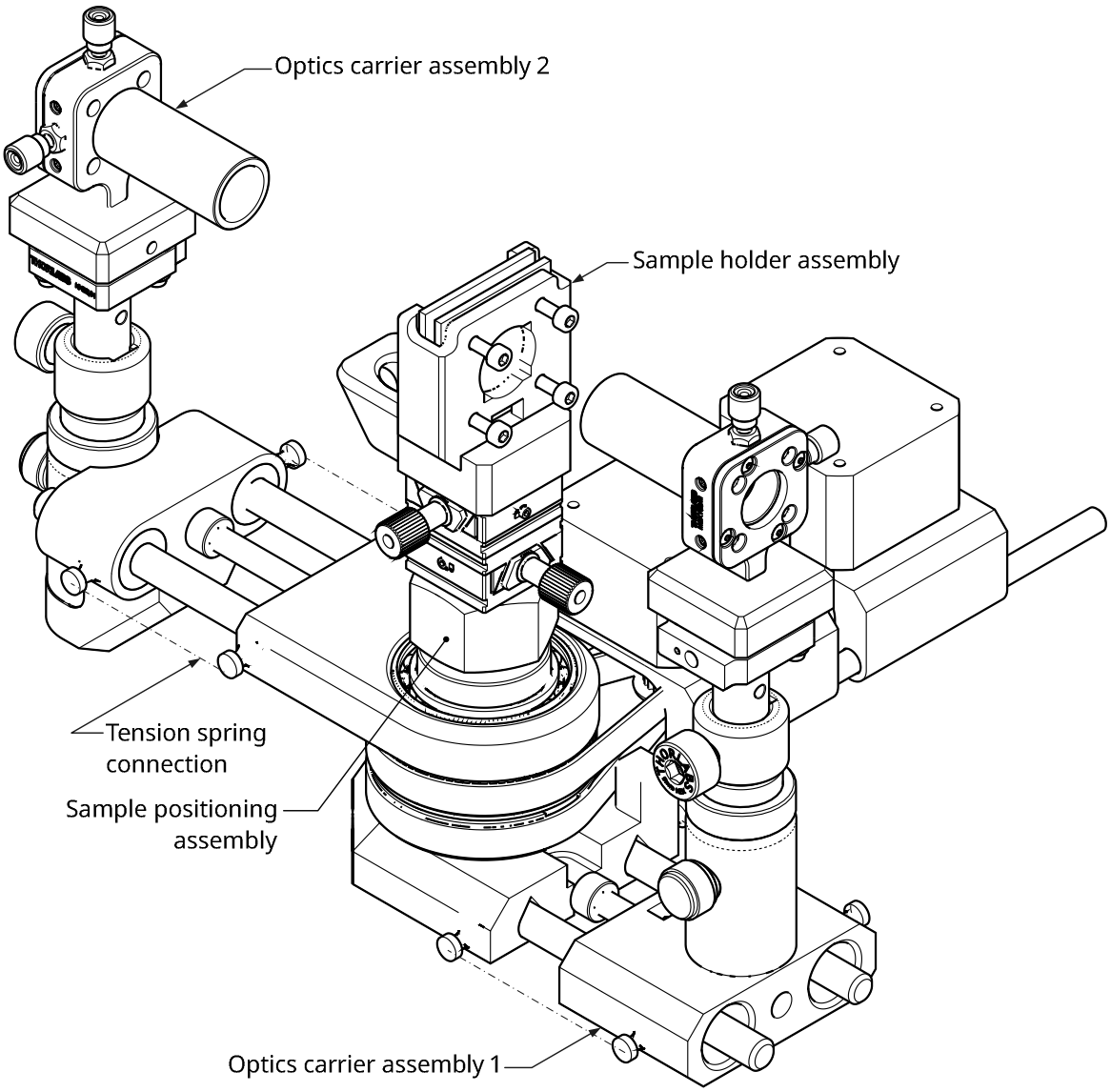

Supplementary Figure 4. Main assembly. Optics carrier assemblies are attached to the main and secondary board shafts, and the sample holder and adjustment system is attached to the main shaft. Not shown are the tension springs that remove backlash from the linear adjustment of the optics carriers.

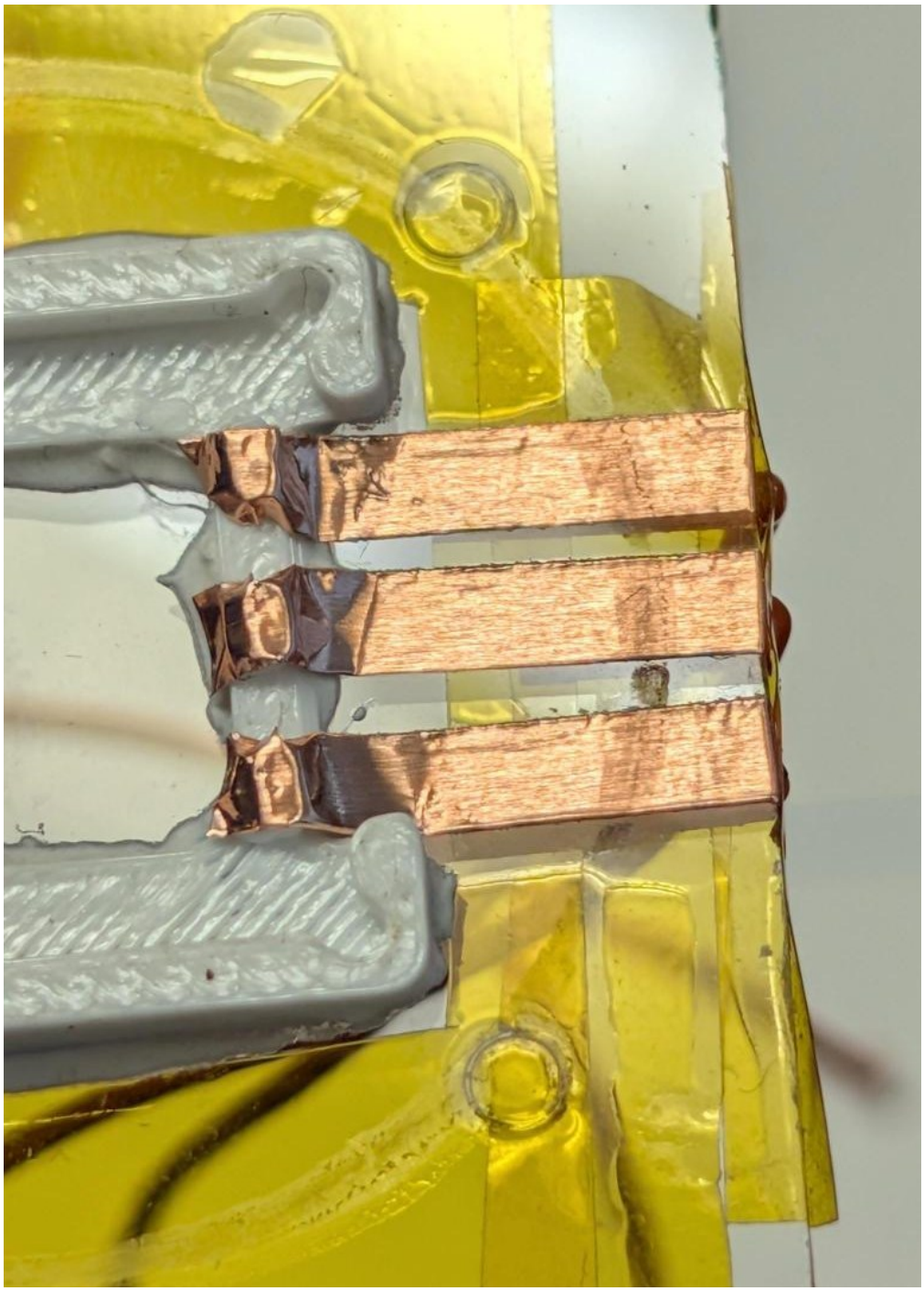

Supplementary Figure 5. Sealing failure due to conductors on the seal contact line. The O-ring that was placed here had a very thin layer of vacuum grease. The amount used was not enough to fill in the gaps explained in Figure 12**Error! Reference source not found.**, and the air gaps free of grease c an be observed adjacent to the conductors.

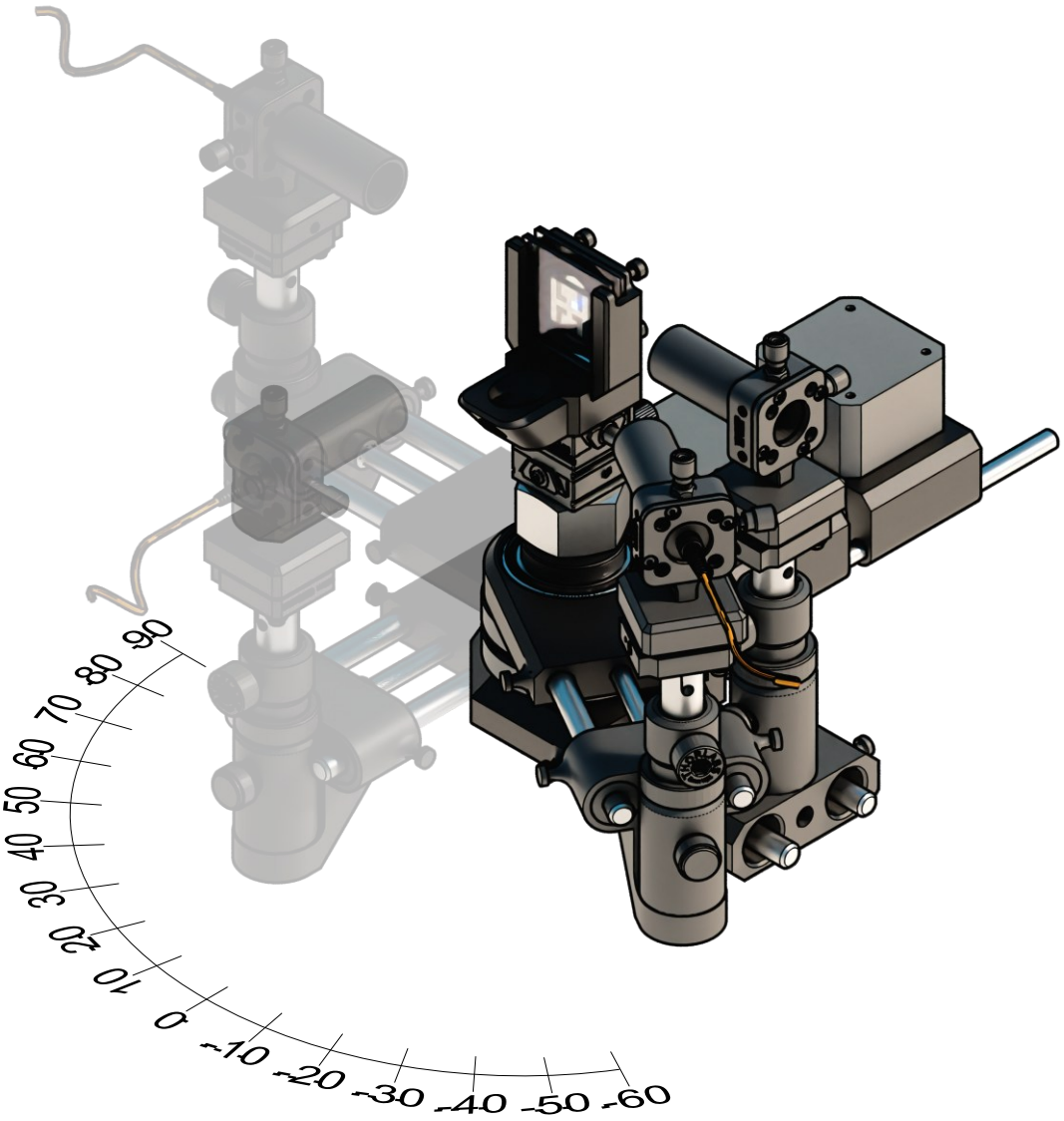

Supplementary Figure 6. Schematic of the EL scan. The scan is started from 90 degrees and ends at -60 degrees. Exposures are taken every 10 degrees at 300 ms exposure times.

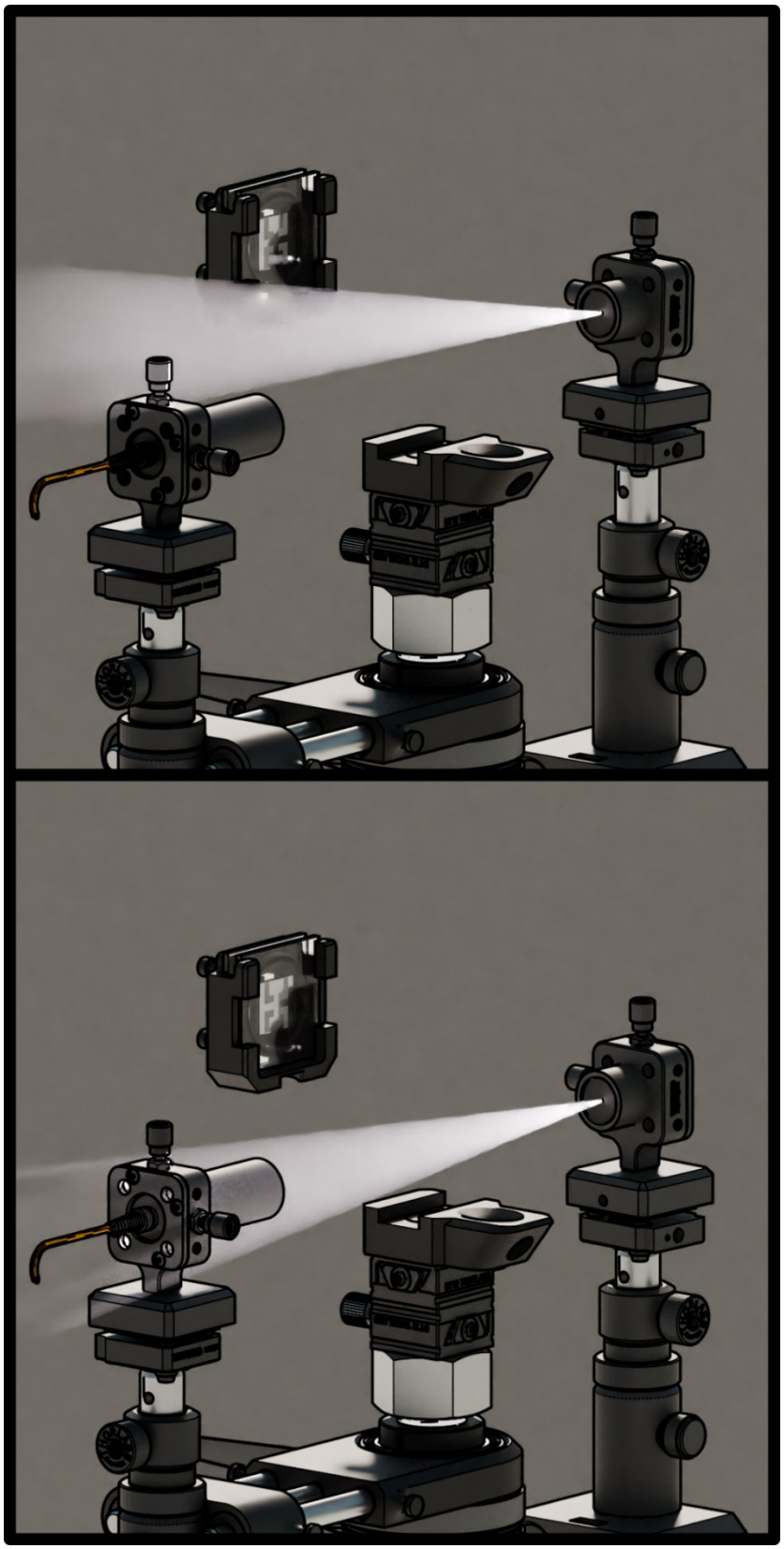

Supplementary Figure 7. Alignment #1: Establishing the primary optical axis. A lens tube with apertures fitted is installed to the excitation side of the device. White light is input with an optical fiber. The beam is walked by adjusting all degrees of freedom sequentially some times over, such that the light intensity seen at the collection optics is maximized. The axis can be more precisely defined by using a second aperture tube attached to the sample holder: this ensures that the beam path is normal to the sample.

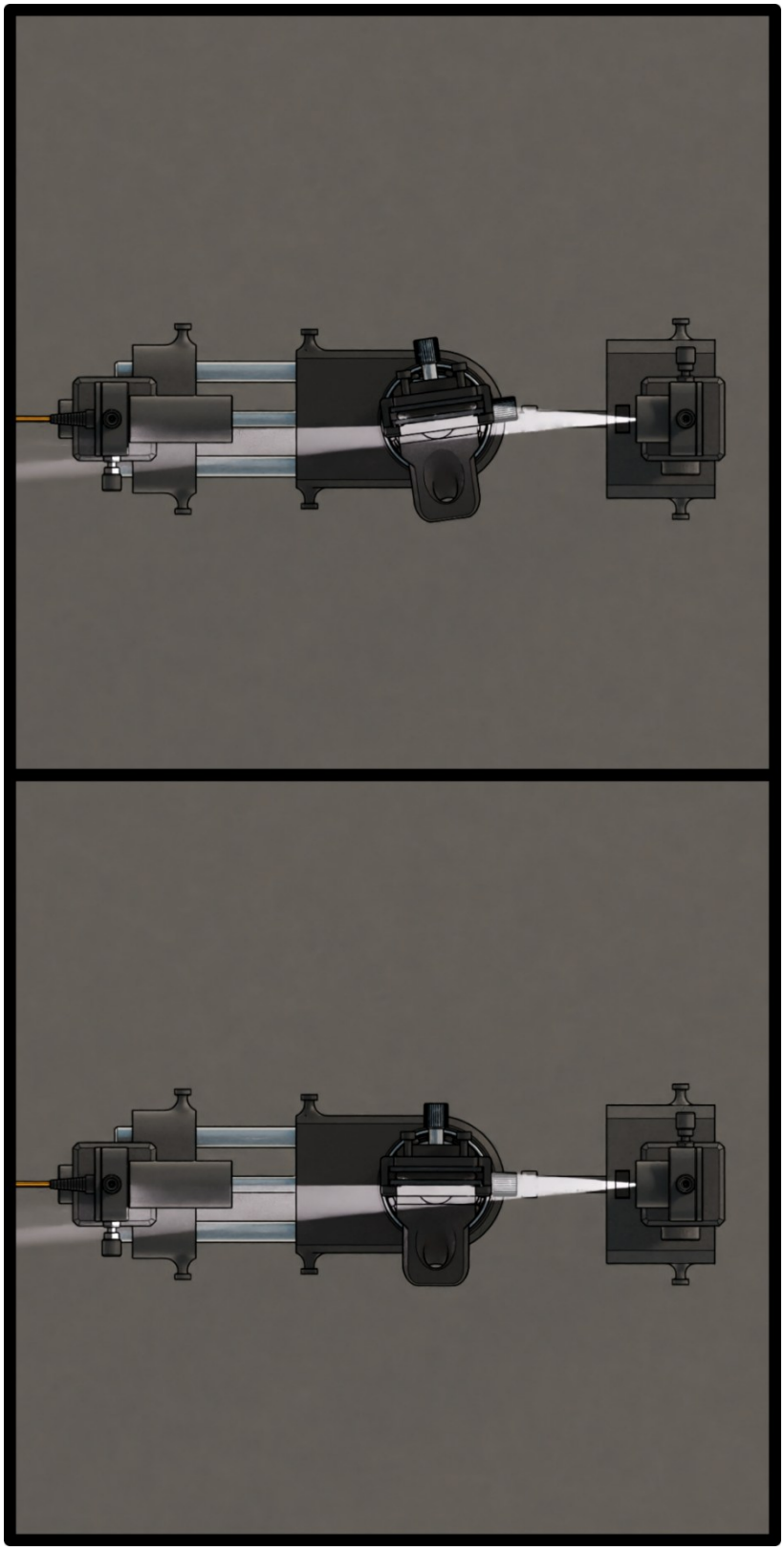

Supplementary Figure 8. Alignment #2: Finding the 90° angle. Once the system has been “factory aligned,” finding the 90° angle becomes trivially easy. The white light maximization technique is used: the motors are rotated back and forth sequentially in software until maximum intensity is achieved.

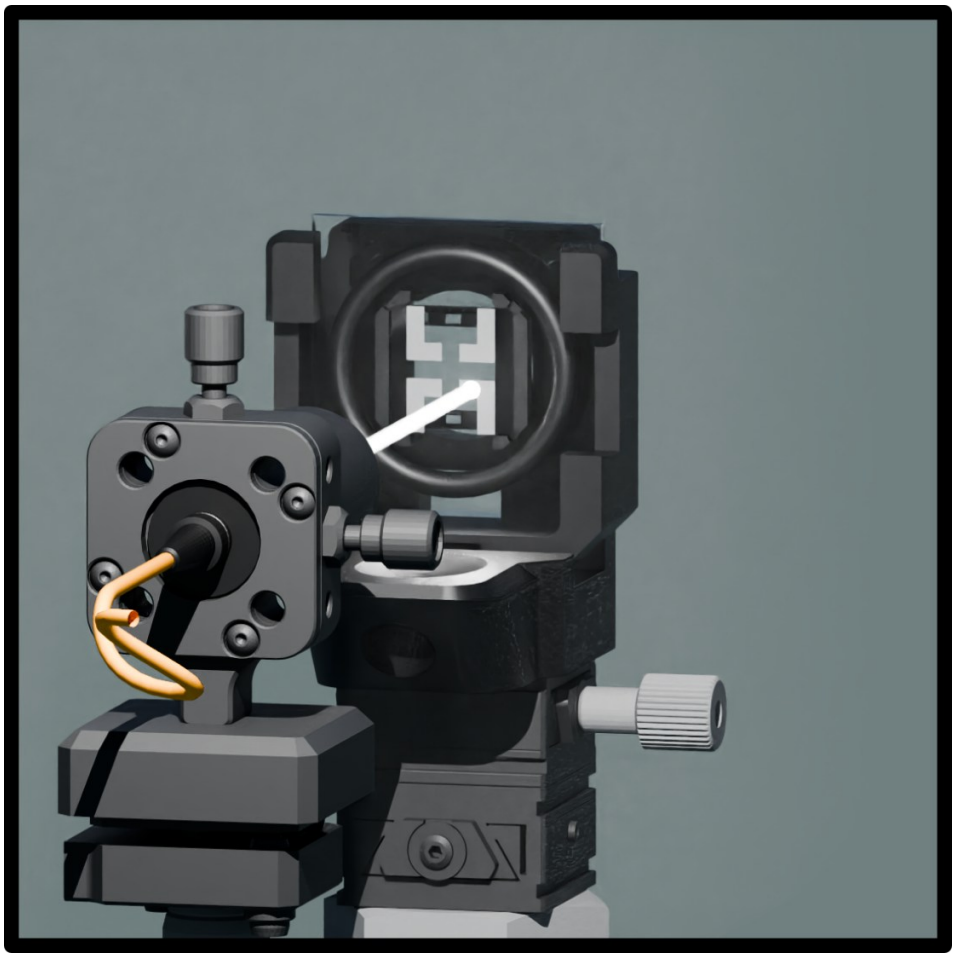

Supplementary Figure 9. Alignment #3: finding the pixel. The spot of light should stay on the pixel as the sample is rotated.

Appendix 2: Data and calculations for electricity consumption and cost claims

European household electricity cost

$$Cost = 3.9 \cdot 10^{11} kWh \cdot 0.24 \frac{€}{kWh} \approx 9.4 \cdot 10^{10} €$$

US electricity cost commercial, manufacturing and total (for lights in 2018)

$$Cost_{comm} = 2.08 \cdot 10^{11} kWh \cdot 0.1067 \$/kWh \approx 2.22 \cdot 10^{10} \$$$

$$Cost_{man} = 5.3 \cdot 10^{10} kWh \cdot 0.0692 \$/kWh \approx 3.7 \cdot 10^{9} \$$$

$$Cost_{total} \approx 2.59 \cdot 10^{10} \$$$

US emissions

$$emissions \approx 463 gCO_2/kWh \cdot 2.61 \cdot 10^{11} kWh \cdot \frac{1kg}{1000g} \approx 1.2 \cdot 10^{11} kgCO_2$$

Monitor power consumption data

Method: Web pages of two local retailers (Gigantti, Verkkokauppa) were visited, products were filtered by “monitors” and “most popular.” The 10 most popular monitors from each retailer were inspected, and their power consumptions in basic operation modes (non-HDR) were averaged.

https://eprel.ec.europa.eu/screen/product/electronicdisplays/1775293?navigatingfrom=qr
Accessed 14/02/2026, 11.33.37

https://eprel.ec.europa.eu/screen/product/electronicdisplays/2278373?navigatingfrom=qr
Accessed 14/02/2026, 11.35.15

https://eprel.ec.europa.eu/screen/product/electronicdisplays/2396482?navigatingfrom=qr
Accessed 14/02/2026, 11.35.25

https://eprel.ec.europa.eu/screen/product/electronicdisplays/1775293?navigatingfrom=qr
Accessed 14/02/2026, 11.35.36

https://eprel.ec.europa.eu/screen/product/electronicdisplays/2342409?navigatingfrom=qr
Accessed 14/02/2026, 11.35.44

https://eprel.ec.europa.eu/screen/product/electronicdisplays/2189091?navigatingfrom=qr
Accessed 14/02/2026, 11.35.55

https://eprel.ec.europa.eu/screen/product/electronicdisplays/2308842?navigatingfrom=qr
Accessed 14/02/2026, 11.36.02

https://eprel.ec.europa.eu/screen/product/electronicdisplays/1950388?navigatingfrom=qr
Accessed 14/02/2026, 11.36.13

https://eprel.ec.europa.eu/screen/product/electronicdisplays/2262201?navigatingfrom=qr
Accessed 14/02/2026, 11.36.20

https://eprel.ec.europa.eu/screen/product/electronicdisplays/1775280?navigatingfrom=qr
Accessed 14/02/2026, 11.36.31

https://eprel.ec.europa.eu/screen/product/electronicdisplays/2360899?navigatingfrom=qr

Accessed 14/02/2026, 11.41.43

https://eprel.ec.europa.eu/screen/product/electronicdisplays/1679910?navigatingfrom=qr
Accessed 14/02/2026, 11.41.47

https://eprel.ec.europa.eu/screen/product/electronicdisplays/2055381?navigatingfrom=qr
Accessed 14/02/2026, 11.41.49

https://eprel.ec.europa.eu/screen/product/electronicdisplays/1560843?navigatingfrom=qr
Accessed 14/02/2026, 11.41.51

https://eprel.ec.europa.eu/screen/product/electronicdisplays/1909394?navigatingfrom=qr
Accessed 14/02/2026, 11.41.53

https://eprel.ec.europa.eu/screen/product/electronicdisplays/2396692?navigatingfrom=qr
Accessed 14/02/2026, 11.41.55

https://eprel.ec.europa.eu/screen/product/electronicdisplays/2235894?navigatingfrom=qr
Accessed 14/02/2026, 11.41.58

https://eprel.ec.europa.eu/screen/product/electronicdisplays/2359466?navigatingfrom=qr
Accessed 14/02/2026, 11.42.00

https://eprel.ec.europa.eu/screen/product/electronicdisplays/2338407?navigatingfrom=qr
Accessed 14/02/2026, 11.42.02

https://eprel.ec.europa.eu/screen/product/electronicdisplays/1965513?navigatingfrom=qr
Accessed 14/02/2026, 11.42.04